Human brain cell types shape host-rabies virus transcriptional interactions revealing a preexisting pro-viral astrocyte subpopulation

Authors

Lena Feige[1,2#,] Karl Young[3], Juan Pablo Cerapio[4-8], Tatsuya Kozaki[9], Lauriane Kergoat[1], Valentina Libri[10], Florent Ginhoux[9,11-12], Milena Hasan[10], Lamya Ben Ameur[3], Gregory Chin[3], Zach Goode[3], Hervé Bourhy[1*] and Arpiar Saunders[3#$*]

[1] Institut Pasteur, Université Paris Cité, Lyssavirus Epidemiology and Neuropathology, F-75015, Paris, France

[2] Université de Paris Cité, F-75015, Paris, France

[3] Vollum Institute, Oregon Health & Science University, Portland, OR, 97239, USA

[4] Centre de Recherches en Cancérologie de Toulouse, INSERM UMR1037, Toulouse, France

[5] Toulouse University, Toulouse, France

[6] CNRS UMR 5071, Toulouse, France

[7] Institut Universitaire du Cancer-Oncopole de Toulouse, Toulouse, France

[8] Laboratoire d'Excellence 'TOUCAN-2', Toulouse, France

[9] Singapore Immunology Network, Agency for Science, Technology and Research, Singapore 138648, Singapore

[10] Single Cell Biomarkers UTechS, Institute Pasteur, 28 rue du docteur Roux, 75015 Paris, France, Université Paris Cité, Paris, France

[11] Shanghai Institute of Immunology, Shanghai JiaoTong University School of Medicine, 280 South Chongqing Road, Shanghai 200025, China

[12] Translational Immunology Institute, SingHealth Duke-NUS Academic Medical Center, 20 College Road, Discovery Tower Level 8, Singapore 169856, Singapore

# equal contribution
$ lead contact
*Correspondence: saundear@ohsu.edu (A.S.), herve.bourhy@pasteur.fr (H.B.)

Keywords: neurovirology, rabies virus, single-cell RNA-seq, host – pathogen interactions, astrocytes, microglial

Summary

How virus-host cell interactions and innate immune antagonism shape neurotropic infection dynamics across diverse brain cell types are largely unknown. To “unmask” and study how innate immune inhibition affects cell type-specific transcriptional regulation of the human and viral genome, we performed single-cell RNA sequencing of human brain cell co-cultures, comparing an isolate of rabies virus (RABV) to its mutant incapable of antagonizing interferon- and NF-κB-dependent responses. RABV gene expression was shaped by host cell type. RABV induced small-scale, cell-type conserved transcriptional programs that likely support infection by 1) hijacking negative transcriptional feedback of pro-viral factors while 2) reducing anti-viral RNAs. Unexpectedly, disinhibited innate immune signaling increased RABV transcription, most strikingly in an infection-independent “pro-viral” astrocyte subpopulation. Further analysis suggested that “pro-viral”-like astrocytes are a rare subtype in the human brain and are primed to protect the brain during viral infection in concert with interferon-sensitive microglia recalcitrant to infection.

Introduction

Viruses possess diverse mechanisms that shape the cellular and molecular properties of host cells through direct viral-host protein interactions. Due to historic technical limitations, the molecular consequences of these interactions have been difficult to characterize, especially across diverse primary cell types that constitute complex tissue such as the human central nervous system (CNS). The neurotropic Rabies virus (RABV) – a prototypic member of the negative-stranded RNA *Lyssavirus* genus – has evolved specialized mechanisms of immune evasion in the CNS, contributing to fatal encephalomyelitis and approximately 60,000 deaths annually[1]. Immune evasion is a critical feature of RABV pathogenesis, as the virus must travel undetected for long distances from peripheral muscle into the CNS, leveraging neurons and neuronal synapses for retrograde (dendrite-to-axon) transport[2]. Remarkably, neuronal viability and function are preserved during infection of non-cell culture adapted RABV strains as brains often show minimal macroscopic and histopathological alterations[3,4]. While neurons possess mechanisms to detect and respond to infection, neuronal immune responses are comparatively restricted to those of neighboring glia[5,6], functionally-distinct brain cell types that form intimate physical interactions with neuronal processes and perform myriad functions. Recent *in vivo* evidence suggests RABV can infect astrocytes and Schwann cells, challenging the notion of exclusive neuron-specific tropism[7–9]. Astrocytes in particular are crucial for IFN-β signaling during RABV infection[10] and can enter "reactive" molecular states in response to diverse insults, including viral infection[11]. Microglia too are involved in RABV pathogenesis[12], but it remains unclear whether viral antigens observed within microglia are due to active infection or because of phagocytosis of infected neuronal material. Despite this unresolved debate, numerous reports indicate microglia transcribe genes involved in innate immunity and signaling (such as *ISG15*, *OASL1*, *IFIT2*, *CCL5*, *CXCL10* and *IL-6*) in response to RABV infection[9,13,14]. Whether these transcriptional responses are driven by direct microglia infection versus cytokine signaling from other cell classes remains unclear. To counteract cellular innate immune pathways, RABV proteins evolved mechanisms to sabotage the *nuclear factor 'kappa-light-chain-enhancer' of activated B-cells* (NF-κB)[15,16] and the Janus kinases (JAK) - Signal Transducers and Activators of Transcription (STAT) pathways[17–20], and thus potently inhibit host cell transcriptional responses downstream of interferon (IFN) type I signaling[21]. Although significant mechanistic insights have been made into immune inhibitory function of RABV proteins using cell lines, the consequences of these physical interactions on properties of infection in neurons and glia are largely unknown. Importantly, many viruses, including RABV, appear to have co-opted host cell proteins (including innate immune detectors[22]) for their life cycle[23], suggesting that infection outcomes may depend on a complex relationship between anti- and pro-viral factors[24], the nature of which remains to be fully elucidated.

In this study, we developed an experimental system using Tha isolate RABV, co-cultured stem cell-derived human brain cell types and single-cell RNA-sequencing (scRNA-seq) to discover how active inhibition of IFN and NF-κB signaling shapes transcriptional responses across the human and viral genomes at single-cell resolution. RABV genes are transcribed by the RNA-dependent RNA polymerase L and the phosphoprotein P complex at levels that reflect the order of the negative stranded RNA genome (3′ N-P-M-G-L 5')[25–27](**Figure S1A,B**). The influence of cell type and state on RABV mRNA levels is unknown.

Of the five RABV proteins, the phosphoprotein (P) and matrix protein (M) potently inhibit key pinch-points in cellular innate immune signaling. Specifically, P protein selectively binds and inhibits phosphorylated targets downstream of IFN signaling, including STAT1/2/3[17–19,28–30] transcription factors in the cytoplasm or nucleus, as well as TBK1 and IKKε kinase[31–33]. M

143 protein binds and inhibits RelAp43[15,16] - an N-terminally truncated isoform of the RelA NF-κB
144 transcription factor - disturbing NF-κB transcriptional complexes (**Figure S1C**). Foundational
145 work has shown that 1) RABV adaptation to cell culture genetically erodes the potency of
146 innate immune inhibition[21] and alters viral tropism *in vivo*[7] and 2) has identified mutations in
147 outward facing residues in P (W265G, M287V; "2P")[34] and M proteins (R77K, D100A, A104S,
148 M110L; "4M")[15] that prevent pSTAT1/2 and RelAp43 binding, respectively, yet leave canonical
149 viral functions intact[20] (**Figure S1D-F**). In response to exogenous IFNα stimulation, Tha RABV
150 completely blocks activation of transcriptional activity of the interferon-stimulated gene (ISG)
151 response element. However, when Tha2P4M mutations are present, transcriptional activation
152 of the ISG response element is equivalent to uninfected cells (i.e. fully disinhibited)[20]. Thus,
153 we sought to "unmask" the otherwise potent innate immune inhibition of Tha virus using its
154 2P4M knock-in mutation counterpart and study the consequences of intact and unmasked
155 innate immunity on viral and host transcriptional signatures across human brain cell types.

156 Our analysis reveals several important discoveries. First, we show that Tha RABV gene
157 transcription is coupled to transcription of the host cell genome and shaped by the host cell
158 type. Second, we demonstrate that Tha virus induces a conserved transcriptional response in
159 both neurons and astrocytes, increasing RNAs encoding proteins that are likely "pro-viral" and
160 thus promoting infection, while decreasing RNAs encoding interferon-related transcription
161 factors that control anti-viral responses. Third, we show, counterintuitively, that 2P4M-based
162 disinhibition of innate immune signaling is associated with an increase in RABV transcription
163 across cell types. Increased viral transcription is most strikingly observed in a subpopulation
164 of "pro-viral" astrocytes, likely enabled by large-scale changes in the astrocytic molecular
165 milieu. These changes include increased transcription of NF-κB effector and interferon-
166 stimulated genes (ISGs) and reduced expression of genes supporting protein translation and
167 mitochondrial function. Additional analysis suggests that "pro-viral" astrocytes are likely a rare
168 subpopulation present in nominally uninfected human brain. Finally, we demonstrate that
169 microglia are almost completely recalcitrant to infection but nonetheless respond to infection
170 of other cell types through an ISG expression response that is potentiated by both higher viral
171 challenge doses and 2P4M mutations. Through the lens of gene expression, our data
172 collectively suggest that innate immune inhibition by isolate RABV maintains infection stealth
173 by restricting viral gene expression, inhibiting the emergence of "pro-viral" astrocyte state and
174 limiting ISG transcription in microglia.

175

176 Results

177 *Discerning infection states and host cell types from single-cell RNA sequencing data*

178 To study how isolate Tha RABV alters the molecular properties of human brain cell types at
179 single-cell resolution - and to "unmask" and then characterize how antagonism of IFN and NF-
180 κB by Tha RABV P- and M-proteins sculpt these changes through regulation of both the human
181 and Tha RABV genome - we performed scRNA-seq analysis (10x Genomics Chromium 3'
182 v3.1) of co-cultured human neurons, astrocytes and microglia 48 hours after bath application
183 of Tha (multiplicity of infection (MOI) 0.5 or MOI 5) or Tha2P4M (MOI 0.5) or from uninfected
184 control wells ("No Infection")(**Figure 1A**). Absolute MOIs were calculated using interferon-
185 response deficient BSR cells yet, when introduced into co-cultures, represent a relative
186 exposure of ten-folder lower or higher number of RABV particles (**Methods**). Brain cell co-
187 cultures were seeded with approximately equal proportions of hNSC-derived neurons and
188 astrocytes (~47% each) as well as a small population microglia derived from human pluripotent

189 stem cells(~6%)(**Methods**). The presence of these differentiated cell classes and Tha RABV
190 infection was confirmed using a Tha virus expressing eGFP followed by immunolabeling of
191 cell-type-specific marker proteins (**Figure 1B**). After quality control, our analysis focused on
192 n=23,457 single-cell RNA profiles derived from acutely dissociated cells with >2,000 RNA
193 transcripts (as defined by unique molecular identifiers; UMIs) collected across multiple
194 biological replicates (No Infection control, n=3; Tha(0.5), n=3; Tha(5), n=2; and Tha2P4M (0.5),
195 n=2)(**Figure S2A,B; Methods**).
196
197 We next sought to accurately distinguish infected cells and uninfected "bystander" cells and
198 assign host cell type identities to each RNA profile. Because infected cells may contain variable
199 levels of viral mRNA, and bystander cells may accrue viral transcripts by chance during cell
200 dissociation and scRNA-seq library preparation, we developed a data-driven computational
201 approach using expectation-maximization to iteratively refine viral RNA distributions for
202 infected and bystander populations, accounting for variability in viral RNAs driven by biological
203 and technical factors (**Figure 1C,D**; **Methods**). The resulting "viral mRNA load" distributions –
204 defined as the percentage of total cellular mRNA derived from the Tha genome – clearly
205 delineated populations of infected and bystander cells (**Figure 1E**). Simulated viral expression
206 data based on these inferred distributions closely matched that of real data, confirming the
207 accuracy of our approach (**Figure S2C**). Throughout this study, we use both qualitative
208 infection categories as well as a quantitative metric of infection progression ("viral mRNA load")
209 to guide our analysis of host and virus gene expression relationships at single-cell resolution.

210 To assign single-cell RNA profiles to transcriptionally-defined brain cell types, we clustered cell
211 profiles using only genes from the human genome (**Methods**). The resulting clusters
212 corresponded to 5 major brain cell populations: neural stem cells (10.7%; n=2,526), mitotic
213 cells 3.3%; n=781), astrocytes (16.9%; n=3,975), microglia (5.2%; n=1,218) and two groups of
214 neurons (*OTP*+ and *SHOX2*+, (31.2%; n=7,312 and 32.6%; n=7,645, respectively) (**Figure 1F**
215 and **Figure S2D**). Each clustered cell population was robustly delineated by hundreds of
216 differentially expressed genes, including well-established "markers" that confirmed cell type
217 identities (**Figure S2E**). Throughout our analysis, we used both OTP+ and SHOX2+
218 populations when analyzing neurons. RNA expression relationships were consistent with a
219 dynamic developmental continuum visible in the two-dimensional UMAP embedding, with a
220 population of hNSCs differentiating into both neurons and astrocytes, as well as a population
221 of markedly distinct microglia, consistent with unique developmental and experimental origin.

222 We next evaluated the type and proportion of infected cells across cell types and Tha RABV
223 infection conditions (**Figure 1G**). While microglia exhibited strikingly low infection percentages
224 across all conditions (~1%), all other cell types exhibited infection percentages between 79.7-
225 91.1% at MOI 0.5 and 96.8-98.4% at MOI 5. We observed no difference in cell-type rate of
226 infection between Tha(0.5) and Tha2P4M(0.5), suggesting that mutations in the RABV P- and
227 M-proteins had little effect on infection probability. Collectively, our scRNA-seq data and
228 analysis framework confirm the tenets of our human cell type co-culture experimental system
229 and enable properties of Tha infection and the consequences of innate immune inhibition to
230 be analyzed at single-cell resolution in the context of host cell type.

231

232 ***Tha2P4M mutations increase viral transcription***

233 We next sought to understand how RABV transcription is shaped by human host cell type and
234 the 2P4M mutations. Because lyssavirus infection involves both negative-stranded RNA

genomes and positive-stranded anti-genomes and transcripts, we first evaluated the genomic locations of our Tha RABV scRNA-seq reads to determine which RNA species were counted in our dataset. Consistent with exclusive mRNA capture and 3' RNA sequencing, we observed sense-read pileups immediately adjacent to viral polyadenylation signals, with negligible sense or anti-sense reads mapped to other genomic locations. As expected, reads from bulk sequencing of whole Tha mRNAs[35] fully covered the five RABV gene bodies (**Figure S3A,B**). Next, we evaluated mRNA-based viral load distributions across cell types and experimental conditions (**Figure 2A** and **Figure S3C**). We observed that mRNA viral load scores did vary by both cell type and experimental condition. Strikingly, Tha2P4M(0.5) infections exhibited a robust, consistent doubling of viral mRNA load across cell types (range of means = 4.8 – 7.7%) as compared to Tha(0.5) and Tha(5) infections consistently (range of means: Tha(0.5), 3.3 – 3.8%; Tha(5), 3.2 – 3.8%. Since the 2P4M mutations do not detectably alter the function of RABV transcription or replication[20], these results suggest cellular changes downstream of the 2P4M mutations (likely through disinhibited IFN and NF-κB signaling) increase rather than restrict viral transcription across cell types. Moreover, a subset of Tha2P4M infected astrocytes exhibited strikingly high viral mRNA load scores (>10%) not observed in other Tha2P4M infected cell types (**Figure 2A**), suggesting 2P4M-disinhibited RABV transcription is especially pronounced in a subpopulation of human astrocytes. Thus one role of wild-type Tha P and M proteins is to indirectly restrict viral mRNA expression as compared to 2P4M mutated proteins.

Tha RABV gene expression is shaped by host cell type and viral mutations that restore host innate immune responses

We next asked whether the levels of *individual* Tha RABV genes are shaped by host cell type and 2P4M mutations, as we observed for aggregate viral mRNA expression. Interestingly, both bulk and scRNA-seq measurements of Tha mRNAs levels were not strictly explained by genome order (**Figure S3B**). *N*, *P*, and *M* were expressed at high levels and *G* and *L* at much lower levels. While cross-gene expression comparisons are potentially influenced by the methodologies used to prepare sequencing libraries, intra-gene expression comparison across scRNA profiles are unaffected by these potential technical artifacts. Therefore, we compared the relative expression of each Tha RABV gene to total viral RNAs across scRNA profiles stratified by cell type and infection condition. Because the accepted "start-stop" transcriptional model includes no role for feedback from host cell type or molecular state, we hypothesized that 2P4M mutations and host cell type should not influence the expression of each Tha gene. In contrast to our hypothesis, we observed influences of both the cell type and the Tha infection condition on relative expression of Tha RABV genes (**Figure 2B** and **Figure S3D**). Most strikingly, across all Tha RABV infection conditions, relative *L* mRNA levels were doubled in neurons compared to astrocytes. While MOI had only a marginal effect on Tha gene expression by host cell type (**Figure S3D**), *N* and *P* levels differed across Tha2P4M infected neurons and astrocytes ($p < 2E-16$; Mann-Whitney test), with neurons having slightly lower levels of *N* and slightly higher levels of *P* mRNAs (**Figure 2B**). These results suggest that the Tha RABV mRNA levels are sculpted by host cell type and 2P4M mutations.

Tha RABV infection induces a cell-type-conserved pro- and anti-viral transcriptional response involving a small number of genes

Viral infections - including by various strains of RABV – can alter transcriptional regulation of the host cell genome in ways that have complex effects on host cell and tissue function[35–37]. However, systematic molecular descriptions of how RABV infection might alter the

282 transcriptome of distinct human brain cell types – including the consequences of innate
283 immune antagonism induced by wild-type P and M proteins – have yet to be described at
284 single-cell resolution. Therefore, we compared genome-wide expression data across cells
285 stratified by cell type and experimental condition to evaluate how Tha RABV infection and
286 2P4M-sensitive innate immune disinhibition shapes neuron and astrocyte-specific
287 transcriptional responses.

288 To characterize transcriptional changes driven by Tha RABV infection and compare these
289 changes across distinct host brain cell types, we performed genome-wide differential
290 expression testing across cell-type-identified scRNA profiles from Tha RABV-infected
291 (Tha(0.5)) versus "No Infection" cells, with a primary focus on neurons and astrocytes (**Figure**
292 **3** and **Figure S4A**; **Table S1; Methods**). Using false-discovery rate corrected p-values (FDR
293 < 0.05) as a threshold, we identified 13 and 60 differentially expressed genes (DEGs) in
294 neurons and astrocytes, respectively (**Figure 3A**). To determine the degree to which
295 transcriptional responses to Tha RABV infection were shared or unique across neurons and
296 astrocytes, we compared gene-specific fold-change values while also tracking gene
297 expression levels in uninfected neurons (**Figure 3B**). Neuron and astrocyte specific responses
298 to Tha-infection were well-correlated (r = 0.64), with a small set of human genes robustly
299 induced in each cell type. Genes with significant reductions in astrocytes also tended to be
300 reduced in neurons, but low neuronal baseline expression likely limited further reductions due
301 to sensitivity of our testing. Shared, strongly induced RNAs include those from *DYNLL1*,
302 *DYNLL2* and *HSPA8* genes and the long non-coding RNA *NRAV* (located in anti-sense
303 orientation in the *DYNLL1* gene locus). DYNNLL1/2 are dynein-light chain subunits that
304 interact with many other cellular proteins, bind RABV P[38–41] and L[42], and promote RABV
305 transcription and replication. *HSPA8* encodes a member of the HSP70 family that is induced
306 upon infection of RABV and other viruses, is sequestered to RABV viral factories and promotes
307 RABV viral transcription and replication[23]. *NRAV* too has described pro-viral functions[43]. RNAs
308 present in lower amounts in Tha RABV infected cells were largely restricted to genes encoding
309 components of the IFN signaling, including *STAT1*, *IRF9*, *IFIT1* and *ISG15*, supporting
310 previous observations that wild-type Tha(0.5) RABV infection condition is sufficient to
311 suppresses IFN-induced expression of innate immune genes encoding detectors and early-
312 stage infection effectors[20] (**Figure S4B**). Gene expression comparisons based on ten-fold
313 higher RABV MOI resulted in highly similar transcriptional changes (**Figure S4A**). These
314 results demonstrate that during Tha RABV infection - in which an average of ~3% of all mRNAs
315 are viral (**Figure 2A**) - neurons and astrocytes tended to share changes in RNA levels from
316 just a handful of genes: increased mRNAs encode host cell factors with previously described
317 or candidate pro-viral functions, while reduced mRNAs encoded IFN-activated anti-viral
318 transducer or effector proteins. In aggregate, these results suggest two functionally distinct
319 transcriptional signatures that likely promote RABV replication in astrocytes and neurons while
320 minimizing innate immune detection and response.

321

322 ***Tha2P4M mutations unmask an astrocyte-specific transcriptional response to infection***
323 To unmask and compare the transcriptional responses inhibited by wild-type Tha P and M
324 proteins across brain cell types, we performed differential expression testing of infected, cell-
325 type-identified scRNA profiles across Tha(0.5) and Tha2P4M(0.5) conditions (**Figure 3C** and
326 **Figure S4A**). We observed 15 DEGs in neurons, 14 of which were upregulated (**Figure 3C**).
327 This upregulated gene set included a subset of those same IFN-related genes that were
328 downregulated in Tha RABV-infected astrocytes (*IRF9, ISG15, SAMD9, STAT1, PLSCR1*),

329 suggesting this downregulation by Tha RABV infection was driven by effects downstream of
330 wild-type P and M proteins. Astrocytes, however, exhibited significant expression changes in
331 445 up or down-regulated genes (**Figure 3C**). Gene-specific fold change comparisons to
332 neurons confirmed that a small subset of the upregulated genes in Tha2P4M-infected
333 astrocytes were cell-type conserved (n=6 of 204), while the vast majority of upregulated genes
334 (n=198 of 204) and nearly all down-regulated genes (n=241) were unique and selective to
335 astrocytes (**Figure 3D**). These results suggest that host brain cell type plays a profound role
336 in the breadth and capacity for transcriptional responses triggered by innate immune signaling
337 pathways that are typically inhibited by wild-type Tha P and M proteins. Analysis of enriched
338 Biological Pathway gene sets in these 445 genes underscored that genes selectively induced
339 in Tha2P4M-infected astrocytes were associated with innate immune response, viral infection,
340 and ISGs (**Figure 3E; Methods**).

341

342 ***A subpopulation of astrocytes endows a pro-viral RNA cellular environment through a***
343 ***massive transcriptional change***

344 We next determined whether the large-scale transcriptional response observed in the grouped
345 comparison of Tha2P4M infected astrocytes was driven by a specific subpopulation of
346 astrocytes. To do this, we clustered astrocyte scRNA profiles from all experimental conditions
347 using exclusively human genes. Our analysis identified a major (Cluster 1: n=3,759 cells;
348 94.6%) and a minor (Cluster 2: n=216 cells; 5.4%) astrocyte population (**Figure 4A**). The
349 experimental composition of Cluster 2 cells strongly deviated from the full dataset, with a 3.5-
350 fold enrichment of Tha2P4M infected astrocytes, yet all experimental conditions, including "No
351 Infection" co-cultures, contributed cells (**Figure 4B**). Cluster 2 was also enriched for infected
352 cells as compared to the full dataset (95% infected versus 68%; p<2.2E-16; Chi-square
353 test)(**Figure 4B**). Based on our previous observation that a subset of astrocytes had
354 particularly high RABV expression (**Figure 2A**), we compared viral mRNA load scores for cells
355 in Cluster 1 and Cluster 2 (**Figure 4A**). On average, viral load scores were 6.3-fold higher in
356 Cluster 2 than in Cluster 1 (**Figure 4C**). We conclude that a subpopulation of transcriptionally
357 unique astrocytes supports very high levels of Tha RABV mRNA expression. Thus, for
358 simplicity, we refer to Cluster 2 astrocytes as "pro-viral", to connote a molecular state
359 permissive for enhanced RABV transcription. While a small proportion of pro-viral Cluster 2
360 astrocytes were observed without infection (~5%), astrocytes tended to adopt this pro-viral
361 molecular state following Tha RABV infection, especially when the 2P4M mutations were
362 present. Pseudotime trajectory analysis suggested that this astrocyte state transition occurs in
363 continuous manner (**Figure S5A-C** and **Methods)**. These results imply that wild-type P and M
364 proteins likely restrict the emergence of the pro-viral astrocyte state during Tha RABV infection.

365 To quantify the magnitude of transcriptional changes distinguishing Cluster 1 and pro-viral
366 Cluster 2, we performed differential expression testing. Our analysis revealed significant
367 alteration in the RNA levels of 8,864 genes, equating to changes in ~38% of all astrocyte
368 expressed genes (Cluster 2 enriched: 2,343 genes; Cluster 2 depleted: 6,521 genes)(**Figure**
369 **4D**). Thus, the pro-viral state likely represents a massive change in astrocyte molecular milieu.
370 Many genes upregulated in pro-viral Cluster 2 showed trajectory-specific expression across
371 the astrocyte state transition in pseudotime, suggesting that the pro-viral state may be
372 transcriptionally dynamic (**Figure S5B**). Interestingly, RNAs from at least 92 genes increased
373 prior to pro-viral conversion (**Figure S5B**). This gene set was two-fold enriched for chromatin
374 regulators as compared to other pro-viral genes (**Figure S5C**)**.** Many of these chromatin
375 regulators control cellular differentiation in other contexts, including transcription factors within

the AP-1 family (*ATF3* , *FOSL1*, *FOSL2*, *JUNB* and *MAFF*[44–49]), outside the AP-1 family (*CREB5*, *CSRNP1*, *EGR2*, *ETS1*, *FOXS1*, *HEY2*, *ISL2*, *KLF5*, *MEF2C*, *NFATC2*, *PBX4*, *TEAD4*[50–76]), the histone variant *CENPA*[77] and the histone modifier *JADE1*[78].

To determine whether high viral mRNA load was more likely the cause or the consequence of pro-viral astrocyte transcriptional state, we performed two complementary analyses. First, we inspected the relationship of pro-viral identities, pro-viral gene expression and viral mRNA load across pseudotime (**Figure S5B**). Acquisition of pro-viral identities and up-regulation of many pro-viral RNAs tended to precede viral mRNA load increases. Second, we repeated differential expression testing after downsampling scRNA profiles such that viral mRNA load distributions were equivalent across clusters (**Figure S5D**; **Methods).** Gene-specific fold change values were highly correlated across the full and downsampled analysis (r = 0.82), with 32% of significant genes shared in both comparisons (**Figure S5E,F**). The vast majority of other genes passing the significance threshold in the full dataset but had similar, non-significant directional changes in the downsampled data (**Figure S5F**), likely due to the drop in test sensitivity from far fewer cells in the analysis (n= 276 versus 3,975 scRNA profiles). These analyses suggest that high viral mRNA load is more likely a consequence rather than cause of the pro-viral state.

We next tested whether the pro-viral state affects the transcriptional coupling between RABV and host cell genome during infection. To do this, we performed a random forest-based regression analysis, using viral mRNA load scores as the dependent variable and 11,943 human genes as independent variables (**Methods**). In neurons and Cluster 1 astrocytes, regression models explained high levels of variance in viral mRNA load (R^2 = 63.7 or 52.8) and both analyses highlighted a privileged role of *DYNLL1* RNA levels in predicting viral mRNA load (**Figure 4E**). In Cluster 2 astrocytes, the regression model explained far less variance (R^2 = 21.6) and *DYNLL1* levels were no longer predictive. Models run without *DYNLL1* explained far less variance in viral mRNA levels for neurons and Cluster 1 astrocytes (R^2 = 39.3 or 32.6) but not for Cluster 2 astrocytes (R^2 = 20.6). Indeed, stratification of scRNA profiles into low, medium and high viral mRNA groups illustrated that *DYNLL1* RNA levels grew with viral mRNA load scores in neurons and Cluster 1 astrocytes but not in pro-viral Cluster 2 astrocytes (**Figure 4F**). These results suggest that the molecular properties of pro-viral Cluster 2 astrocytes fundamentally alter the transcriptional coupling between RABV and host cell genome, including the typical strong association between *DYNLL1* RNA and RABV transcriptional output.

Identification of pro-viral Cluster 2-like astrocytes in the human brain

The presence of ~5% of uninfected astrocytes in Cluster 2 (including eight “bystander” uninfected astrocytes and two astrocytes from the “No Infection” condition), hinted that this pro-viral astrocytic transcriptional state might exist independent of RABV infection and motivated us to explore the possibility that Cluster 2-like astrocytes might be present in human brains. To evaluate this possibility, we took advantage of a snRNA-seq dataset acquired from flash-frozen cortical tissue resected during Normal Pressure Hydrocephalus (NPH) surgery[79], enabling analysis of *ex vivo* astrocyte RNA profiles from 52 living patients. Therefore, these cortical samples were collected without the confound of post-mortem interval nor acute central nervous system infection. To search for Cluster 2-like astrocytes in the 82,634 NPH snRNA-profiles from astrocytes, we developed an aggregate expression score approach, leveraging genes highly enriched (> 2 log2 fold-change) in pro-viral Cluster 2 astrocytes to create a “discovery” gene set (**Figure 4G,H**; **Methods**). As expected, aggregate expression of this Cluster 2 “discovery” gene set (n=268 genes) clearly distinguished Cluster 1 and Cluster 2

422 scRNA profiles in a manner independent from our original analysis, confirming the approach's
423 sensitivity (**Figure 4G**). We then calculated aggregate expression scores for NPH astrocyte
424 snRNA-seq profiles based on the 196 "discovery" genes expressed in both datasets. To
425 contextualize the distribution of "discovery" gene set scores and define a false-discovery
426 threshold, we performed a similar analysis on n=1,000 permuted gene sets of 196 genes
427 matched for expression level. We then calculated gene set-specific z-scores to directly
428 compare the "discovery" and permutation results (**Figure 4H**; **Methods**). In support of Cluster
429 2-like astrocytes present in living human cortex, we observed a small number of snRNA profiles
430 with very high "discovery" set z scores (up to 12.5 standard deviations above the mean) not
431 observed in the permutations. Using a z-score threshold of 4.5 (corresponding to a p value cut
432 off of 4.7E-7 based on the permutations), we identified n=38 Cluster 2-like astrocytes
433 contributed by 21 of 52 total patients (n=1 to 4 Cluster 2-like NPH astrocytes per patient,
434 ranging from 7 to 4,990 total astrocyte snRNA profiles per patients (median: 1,278). We
435 reasoned that if these 38 single-nucleus RNA profiles were indeed Cluster 2-like, they should
436 also be enriched for an independent gene set with enriched expression in pro-viral Cluster 2
437 astrocytes. Indeed, a "validation" gene set of 521 genes with RNAs 1-2 log2 fold-enriched in
438 Cluster 2 astrocytes also had enriched expression in the 38 snRNA-profiles as compared to
439 all other NPH astrocytes (n= 82,596: $p < 2E-16$, chi-square test). The degree of "discovery"
440 and "validation" gene set enrichment in NPH astrocytes corresponded to the predictions from
441 pro-viral Cluster 2 astrocytes (NPH expression enrichment: "discovery", 2.8; "validation",
442 1.2)(**Figure S5G**). Collectively, these analyses provide preliminary support for a rare (~1 in
443 2,200) population of pro-viral Cluster 2-like astrocytes in human cortex without acute infection
444 of the central nervous system (**Figure S6A,B**).
445
446
447 ***Transcriptional analysis identifies major cell-autonomous and nonautonomous***
448 ***functional changes of pro-viral astrocytes***
449 We next sought to analyze how the massive transcriptional changes distinguishing Cluster 1
450 from pro-viral Cluster 2 astrocytes might alter both intercellular interactions with other cell types
451 and cell-autonomous astrocyte function. Importantly, we found no evidence that the pro-viral
452 transcriptional state we observed in Tha2P4M infected human astrocytes was previously
453 documented in cultured or *ex vivo* rodent and human astrocytes experimentally driven into
454 "reactive" states through interferon[80,81] or lipopolysaccharide exposure (**Figure S7A**).
455
456 To understand to what degree the pro-viral transcriptional state affects astrocyte signaling with
457 other co-cultured brain cell types, we leveraged CellPhoneDB(v5.0), a database of pairwise-
458 protein interactions that includes both secreted and extracellular ligands in relationship to
459 receptor complexes. We focused our analysis on genes with > 1 log2 fold-enrichment in either
460 Cluster 1 (n=2,186) or Cluster 2 (n=877). CellPhoneDB uses cell-type-assigned scRNA-seq
461 data and a gene-shuffling permutations to identify "relevant" ligand-receptor interactions that
462 are selectively enriched in target gene sets over background expression in other cell types (p
463 < 0.05 based on permutations). CellPhoneDB analysis revealed that pro-viral Cluster 2
464 astrocytes tended to express fewer "relevant" ligand and receptor genes than Cluster 1
465 astrocytes, suggesting a global reduction in the capacity for intercellular signaling (**Figure 5A**).
466 Interestingly, the more minor subset of ligands upregulated in pro-viral astrocytes include
467 immune effectors that function as secreted chemokines (*IL34*, *LIF*, *EDN1*) or extracellular
468 glycoproteins (*VCAM1* and I*CAM1*). In some cases, ligands or receptors from the same
469 signaling family exhibited bi-directional changes in RNA levels. For example, *WNT3A* and

470 *VEGFA* (ligands) and *EPHA4* (receptor) were enriched while *WNT7B* and *VEGFB* (ligands)
471 and *EPHB1* (receptor) were reduced in pro-viral Cluster 2 Astrocytes. Analysis of "relevant"
472 ligands and receptors in the context of RNAs expressed by other co-cultured brain cell types
473 suggested that pro-viral Cluster 2 astrocytes (as compared to Cluster 1 astrocytes) exhibit
474 reduced signaling capacity to all major cell types to approximately the same degree. These
475 data also imply that pro-viral Cluster 2 astrocytes are more "cut-off" from receiving interactions
476 from other cell types (save from other pro-viral and Cluster 1 astrocytes)(**Figure 5B**). These
477 inferences based on RNA levels may suggest that pro-viral Cluster 2 astrocytes are poised to
478 send and receive fewer total cellular interactions yet highlight a small number of key pathways
479 through which astrocytes in the pro-viral molecular state might signal to other brain cell types.
480
481 We next leveraged gene expression changes to build testable hypotheses for how the pro-viral
482 transcriptional state might affect cell-autonomous function of human astrocytes. Pro-viral
483 Cluster 2 astrocytes expressed higher levels of annotated human innate immunity
484 genes[82] (n=837) including those stimulated by IFN (n=244) (**Figure S7B,C**). To find additional
485 themed structure in the ~38% of astrocyte-expressed genes differentially expressed across
486 Cluster 2 and Cluster 1 astrocytes, we performed hierarchical clustering of REACTOME
487 categories based on shared genes up regulated in Cluster 1 (n=6,521 genes; n=84 categories,
488 p <1E-6) or Cluster 2 (Cluster 2, 2,343 genes; n=32 categories, p<1E-3)(**Figure 5C**). These
489 results implicate a diverse set of cellular processes affected by the large-scale restructuring of
490 the pro-viral astrocyte transcriptome. Due to the number and complexity of these changes, we
491 focused further analysis on the following salient gene sets to more fully understand how
492 astrocytes in particular respond to infection: 1) genes controlled by "Toll-like receptor
493 cascades" (**Figure 5D**) and genes encoding machinery for 2) protein translation and 3)
494 mitochondrial respiration (**Figure 5E**). ("Toll-like receptor (TLR) cascades" is likely a proxy for
495 gene sets activated by the IRF3/IRF7/NF-κB transcription factor complex, which in the case of
496 RABV infection, is primarily driven through activation of viral sensors such as TLRs and RIG-
497 I-like receptors (RLRs)[83,84]).
498
499 To determine how the molecular milieu of Cluster 2 astrocytes is sculpted by RNA level
500 changes of genes controlled by "Toll-like receptor cascades", we ranked fold-changes for 108
501 associated genes (**Figure 5D**). This analysis highlighted the striking role for transcriptional
502 induction of both NF-κB and immediate early gene (IEG) transcription factors and regulators
503 (NF-κB: *NFKB1*, *NFKB2*, *NFKBIA*, *NFKBIB*; IEG: *JUN*, *FOS*) as well as induction of gene
504 targets controlled by both NF-κB and IEG transcriptional complexes (NF-κB: *BIRC3*, *BIRC2*,
505 *NOD2*, *RIPK3*, *IRAK1, TRAF2;* IEG: *DUSP4, DUSP6, DUSP3*). RNAs from this group with
506 lower relative levels in the pro-viral state encode MAP kinases and regulators (*MAP2K6*,
507 *MAPK10*, *MAPK3*, *MAPK14*, *MAPKAPK3*, *MAPK8*, *MAPK7*) as well as ubiquitin and ubiquitin
508 regulators (*UBB*, *UBA52*, *UBE2V1*, *UBC*, *UBE2D1*, *UBE2N*, *UBE2D2*). Thus, viral sensor
509 activation may contribute to the pro-viral state through relative increases of NF-κB genes and
510 targets and relative reductions of RNAs that might alter MAPK kinase activity and ubiquitin-
511 based protein degradation.
512
513 To determine how transcriptional alterations of genes encoding protein translation and
514 mitochondrial function might contribute to the function of pro-viral astrocytes, we assessed
515 expression-level changes of ribosomal subunits, tRNA synthetases and the COX and NDUF
516 gene families encoding Complex IV and Complex I of the electron transport chain, respectively
517 (**Figure 5E**). Pro-viral astrocytes exhibit potent reductions in RNAs encoding nearly all subunits

of the cytosolic ribosome (n=85 genes), and bi-directional regulation of mitochondrial ribosome subunits (n=78) and tRNA synthetases (n=37 genes). Most members of the COX and NDUF gene families had reduced expression in pro-viral astrocytes. These transcriptional changes were highly-selective for pro-viral astrocytes, as RNA levels associated with these genes were not different across No Infection and Tha(0.5) RABV infected astrocytes (**Figure 5E**). These results suggest that pro-viral astrocytes likely have severely reduced or dysregulated capacity for protein translation and oxidative phosphorylation, potentially indicating a mechanism of "host shut off" based on RNA level changes. Tha RABV infection with wild-type P and M protein efficiently inhibit these changes.

Microglia indirectly respond to infection of other cell types through interferon-stimulated genes potentiated by 2P4M mutations

Lastly, we explored how RABV infection-resistant microglia indirectly respond to infection properties of other susceptible co-cultured brain cell types and how these transcriptional responses associate with Tha RABV titer or innate immune signaling disinhibited by 2P4M mutations. To do this, we re-clustered microglia scRNA-seq profiles and tracked the experimental origins of each library (**Figure 6A**). Three distinct analysis or visualization approaches – including UMAP embeddings (**Figure 6A** and **Figure S8A**), principal components analysis of shared expression variance (**Figure 6B** and **Figure S8B**) and differential expression analysis (**Figure S8C**) – revealed that exposure to Tha RABV particles and the milieu of neighbouring infected cells affect a graded transcriptional response of interferon-induced genes in microglia (e.g. *SNX10*, *GBP1*, *IFIT2*, *ACSL1*)(**Figure 6B**). The number and degree of interferon-induced transcriptional differences were largest in the Tha(5) condition, followed by Tha2P4M(0.5) and then Tha(0.5)(**Figure 6B-D** and **Figure S8C**), as evidenced by example genes (*ISG15, IDO1, and IFIT3*)(**Figure 6E**). Consistent with rapid induction and degradation[85], RNAs encoding interferon proteins were not detected 48 hours after viral infection, obfuscating the cellular source of interferons in our analysis. Importantly, in titer-matched experiments, the interferon-related transcriptional response in microglia was larger with 2P4M mutations (**Figure 6C**), suggesting that disinhibited innate immune signaling and/or higher levels of viral RNA in other cell types potentiate an interferon-stimulated gene responses in microglia. However, analysis of cytokine gene RNA levels in neurons and astrocytes found little support for this model (**Figure S8D**). The majority of cytokine ligand and receptor RNAs were expressed at high levels in microglia themselves (**Figure S8E**). In many cases, both ligands (e.g. *CCL3*, *CCL4*, *CCL5*, *CCL8* and *IL1B*) and receptors (e.g. *CCR5*, *CCR1*, *IFNGR1* and *TNFRSF1A*) were expressed across experimental conditions in a manner similar to ISGs (**Figure S8F**).

Discussion

In this work, we characterized how the innate immune signaling inhibition conferred by RABV P and M proteins shapes the transcriptional properties of the host and viral genomes across human neurons and glia. While molecular mechanistic analyses in cell lines have described the potent and synergistic ways that RABV M and P proteins inhibit the induction and response to IFNs[17–19,28–31], the consequences of innate immune inhibition or disinhibition on host-virus relationships were unknown. Here we used an experimental and analytical framework with several key attributes to characterize these consequences in major human CNS cell types, revealing important new insights into RABV-host cell interactions and how innate immune

566 antagonism shapes viral infection properties. These attributes include 1) the use of Tha RABV
567 derived from a field isolate (that exhibits profound innate immune inhibition as compared to
568 attenuated RABV strains more adapted to cell culture) and 2P4M mutations (that selectively
569 and potently strip away major RABV innate immune inhibitory mechanisms); 2) co-cultured
570 human stem-cell derived brain cell types, enabling human cell biology to be studied in a
571 relevant model of cross-cell type signaling; 3) single-cell RNA-seq phenotyping in which mRNA
572 level across the RABV and human genomes are measured at cellular resolution; and 4) novel
573 analytical methods to qualitatively group infected and uninfected scRNA-seq profiles across
574 heterogenous infection states and the use of "viral mRNA load" as a quantitative proxy for
575 infection state progression. (Viral mRNA load varied considerably in infected cells after 48
576 hours, from 0.4 to 65% viral mRNA, highlighting the importance of tracking viral mRNA load
577 when experimentally phenotyping individual cells). Viral mRNA load distributions suggested
578 no evidence of secondary RABV infections, consistent with the slower replication rates
579 associated with isolate RABV and primary brain cells.

580 Our results suggest two ways in which Tha RABV gene expression is not anticipated by the
581 accepted "start stop" transcriptional model. First, in both bulk mRNA and scRNA-seq based
582 datasets, Tha RABV mRNA levels were not strictly explained by genome order, with *N*, *P* and
583 *M* levels high (~24-46% of viral mRNAs) and *G* and *L* levels much lower (~1-2%). While mRNA
584 capture and library preparation methods can complicate cross-gene RNA level comparisons,
585 the lack of strict genome-ordered expression across independent methods suggests other
586 factors (such as post-transcriptional regulation) may need to be considered to fully understand
587 variable levels of RABV transcripts in infected cells. Second, scRNA-seq analysis suggests a
588 clear if subtle role for host cell type in shaping RABV gene expression. Most saliently, *L* mRNAs
589 were observed on average at double the levels in neurons as compared to astrocytes,
590 differences that could be driven by either molecular or physiological differences in host cells.
591 Future experiments are warranted to fully validate and understand the functional
592 consequences of cell-type-specific RABV gene expression differences and to identify the
593 mechanisms driving these effects.

594 In Tha RABV-infected neurons and astrocytes, we discovered largely conserved bi-directional
595 transcriptional programs involving ~60 human genes that may promote infection progression
596 by both boosting RNAs encoding known pro-viral proteins or reducing RNAs encoding anti-
597 viral transduces or effectors. For example, of the four genes robustly induced by Tha RABV
598 infection (*DYNLL1, DYNLL2, NRAV and HSPA8;* **Figure 3A***),* all have been shown to promote
599 viral replication in some contexts[42]. Importantly, the products of the protein-coding genes
600 (DYNLL1, DYNLL2 and HSPA8) are bound and/or sequestered by RABV proteins during
601 infection. DYNLL1/DYNLL2 were originally described as light-chain dynein subunits but are
602 now appreciated as "hub" proteins that perform myriad cellular roles through hundreds of
603 unique binding partners[86,87]. DYNLL1/DYNLL2 are targeted by RABV P[38–41] and L[42] as well as
604 proteins from diverse other viruses[88]. The long non-coding RNA *NRAV* spans exons 2 and 3
605 of *DYNLL1* gene locus in the anti-sense orientation on chromosome 12 and promotes
606 influenzae replication and virulence[43]. The functional effects of *NRAV* on RABV pathogenesis
607 are yet to be determined. *HSPA8* encodes a member of the HSP70 family, a host cell protein
608 recruited to RABV Negri Bodies (the specialized viral organelles in which viral transcriptional
609 and replication occur) and promotes RABV replication[89]. Our data thus suggest that RABV
610 (and perhaps other viruses) evolved to sequester host cell factors transcriptionally regulated
611 by hijackable negative feedback systems, enabling pro-viral host factor production to match
612 viral demand as infection proceeds. Indeed, our analysis demonstrated that, compared to

613 thousands of other human genes, *DYNLL1* mRNA levels uniquely scale with viral mRNA load
614 in neurons and Cluster 1 astrocytes (**Figure 4E,F**). Previous work has identified a potential
615 mechanism: DYNLL1 sequestration by P and L might disinhibit DYNLL1-based negative
616 regulation of the ASCIZ transcription factor which promotes *DYNLL1* transcription[90]. More
617 experiments are required to understand these transcriptional feedback systems, including the
618 mechanism through which *HSPA8* RNA levels are increased following RABV infection. The
619 genes potently downregulated by Tha infection include RNAs encoding proteins with central
620 roles in anti-viral responses. These include anti-viral effectors IFIT1 and ISG15, as well as core
621 components of the ISGF3 transcriptional complex (STAT1 and IRF9) responsible for inducing
622 interferon expression[91]. These results offer insight into the mechanisms through which Tha
623 RABV infection completely blocks interferon-stimulated gene expression, even after
624 exogenous IFNα stimulation[20]. While more work is necessary to determine exactly how anti-
625 viral RNAs are reduced during Tha RABV infection, wild-type P and M proteins are likely
626 involved, as an overlapping anti-viral gene set is strikingly induced in neurons infected by
627 Tha2P4M (**Figure 3C**).

628 One major observation of our study is that 2P4M-based disinhibition of innate immunity results
629 in a mean doubling of viral mRNA load across infected cell types (**Figure 2A** and **Figure S3C**).
630 Three pieces of evidence suggest that increased viral transcription is an indirect effect of the
631 disinhibited innate immune milieu rather than a direct effect of the 2P4M mutations on the
632 efficacy of the viral transcription complex involving P protein and the RNA-dependent RNA
633 polymerase L. First, the 2P4M mutations sit at residues independent and distant from those
634 known to bind or modulate L function[15,20,92] (**Figure S1D-F**). Second, Tha and Tha2P4M have
635 indistinguishable replication properties in BSR-T7 cells that lack an IFN response[20]. Third, P/M-
636 based restriction of RABV transcription is cell type and state-specific, as observed in the "pro-
637 viral" astrocyte subpopulation, which had on average six-fold higher viral mRNA load scores
638 than other neurons and astrocytes (Cluster 2; **Figure 4A,C**). Therefore, one important
639 consequence of RABV innate immune inhibition is likely to restrict viral transcription.

640 Our discovery and characterization of "pro-viral" human astrocytes deepens the growing
641 appreciation of how astrocytes contribute immune functions in the human CNS[11,93,94] including
642 as viral reservoirs[95–98]. Our *in vitro* analyses suggest that the "pro-viral" molecular state is
643 transcriptionally dynamic and collectively involves ~38% of astrocyte expressed genes. Four
644 lines of evidence suggest that the "pro-viral" state can exist independently of RABV infection
645 and that this state is more likely the cause rather than the consequence of high viral mRNA
646 load: 1) The presence of 5% uninfected "pro-viral" astrocytes (including those from uninfected
647 culture wells); 2) Changes in the levels of many "pro-viral" genes that precede the transition
648 into "pro-viral" Cluster 2 identities and or do not scale with viral mRNA load. These "early"
649 genes include transcription factors and other chromatin modifiers known to control cellular
650 differentiation in other systems; 3) the observation that "pro-viral" gene expression signatures
651 remain after controlling for viral load differences; and 4) the presence of "pro-viral"-like single-
652 nucleus RNA profiles sampled from cortical biopsies of presumably RABV free NPH surgical
653 patients (~1 out of 2,200; observed in 21 of 52 patient samples). Importantly, Tha RABV
654 infection marginally increases the probability of transition into the pro-viral state and that
655 probability is dramatically increased when the 2P4M mutations are present (**Figure 4A,B;**
656 **Figure S5B; Figure S6A,B**). These data may suggest that inhibition of pro-viral astrocyte state
657 emergence during infection is an important feature of RABV innate immune inhibition in the
658 human CNS.

659 We leveraged gene expression data to draw a preliminary description of how the large-scale
660 "pro-viral" state might affect astrocyte function and cellular interactions. Our analysis suggests
661 that the "pro-viral" state tends to reduce the number of molecular opportunities for cell signaling
662 to other brain cell types and the only unique interactions "pro-viral" astrocytes are poised to
663 receive are from other astrocytes (in contrast to other infected astrocytes, which maintain
664 receptors to interact with all other cell types in our co-cultures). Our analysis highlights a
665 number of key signaling molecules including both ligands (*HBEGF4*, *VEGF4*, *IL34*, *VCAM1*,
666 *ICAM1*, *WNT3A* and *EDN1*) and receptors (*EPHA4*, *SSTR2*) that merit further investigation for
667 "pro-viral" astrocyte function[99]. Cell autonomously, "pro-viral" gene expression changes
668 indicate a dramatic increase in ISG and NF-κB target gene expression, predicted to alter MAPK
669 function and protein ubiquitination, among other changes. We also observed cellular mRNA
670 level changes consistent with potent reductions in ribosomal machinery for protein translation
671 and mitochondrial machinery for oxidative phosphorylation. The changes could reflect an
672 astrocyte-specific form of "host shut off". (To our knowledge, "host shut off" molecular programs
673 have not been previously described either in astrocytes or for RABV infection of any cell type).
674 The uncoupled transcriptional feedback between *DYNLL1* levels and viral mRNA observed in
675 "pro-viral" astrocytes (but not in other cell types) may be an important feature of this process
676 (**Figure 4E,F**). Astrocyte-based abortive infections occur at higher frequency in lab-attenuated
677 versus field isolate RABVs[100]. Thus, it will be important to explore whether the "pro-viral" state
678 we observed at higher rates following Tha2P4M infection might represent a transcriptional
679 snapshot of the abortive infection process[58]. High levels of viral mRNA and with reduced
680 protein translation could in theory help "pro-viral" astrocytes create an immune-stimulatory
681 environment through viral RNA while minimizing the generation of infective virions. More work
682 – including through astrocyte infection fate-mapping experiments – is necessary to clarify the
683 functions of key pro-viral state genes and whether the pro-viral state supports abortive
684 infections or other outcomes[101].

685 Our study also sheds a new light on the role of microglia. Our analysis suggests that microglia
686 are almost exclusively recalcitrant to RABV infection (~1% infected, n = 10 of 859; **Figure 1G;**
687 **Figure S8A**). The susceptibility of human microglia to RABV infection has been a topic of
688 scientific debate[37,102,103]. Our findings indicate that human microglia do not play major roles in
689 the replication and spread of dog-adapted RABV (the major cause of RABV infection in
690 humans). The presence of viral mRNAs in the 1% of microglia we classified as infected may
691 also be attributed phagocytosed material from infected cells. Further, the degree of microglial
692 interferon-induced transcriptional differences was largest in the Tha RABV(5) condition,
693 followed by Tha2P4M(0.5) and then Tha RABV(0.5)(**Figure 6** and **Figure S8C**) a signature
694 that could not be simply explained by cytokine expression in neurons and astrocytes (**Figure**
695 **S8D-F**). These results may suggest that graded microglia ISG and cytokine responses may be
696 controlled through sensing of RABV pathogen-associated or danger-associated molecular
697 patterns (PAMPs and DAMPs). These data are consistent with model in which microglia ISG
698 and cytokine RNAs are primarily driven by transient interferon release by other brain cell types
699 or direct microglia sensing of RABV-associated molecular patterns without direct infection. The
700 larger ISG responses microglia in the Tha2P4M(0.5) versus Tha(0.5) conditions could reflect
701 2P4M-dependent increases in free RABV particles (a potential source of PAMPs/DAMPs) in
702 media or signaling responses downstream of 2P4M infections in other cell types. Future
703 experiments should directly test these hypotheses including the identification of possible
704 signaling pathways responsible for RABV recognition by microglia.

Our study has important limitations and follow-up studies are necessary to more fully understand the biological results we reveal. For example, our genome-wide molecular phenotyping was restricted to polyadenylated RNA levels. To more fully understand the molecular consequences of isolate RABV infection and "unmasked" innate immune signaling, single-cell measurements of RABV negative-stranded RNA genomes, full-length host and viral RNA isoforms, and non-coding RNAs (including RABV leader and trailer RNAs) will need to be measured. While the 2P4M mutations profoundly disinhibit innate immune signaling[20], this disinhibition may be incomplete. For example, the serine at residue 179 of P has been shown to be necessary for sequestering IKKε kinase - a key regulator that controls interferon transcription by activating the IRF3/7 transcription factors – and this serine is present in both wild-type P and the 2P mutant. Additionally, more work is required to fully understand the function of "pro-viral" astrocytes and the roles contributed by specific genes induced in the pro-viral state. Future experiments should 1) locate and quantify "pro-viral" astrocytes through molecular anatomical analysis of human brain tissue; 2) characterize the temporal progression and fate of the "pro-viral" state across different conditions (infection both other viruses, aging and neurodegeneration, for example) and 3) functionally assess how the "pro-viral" state affects astrocyte physiology, cell signaling and nuclear chromatin organization. Finally, it is unknown if pro-viral astrocytes are present in other species. Discovery of a similar astrocyte state in mouse, for example, would present a powerful opportunity for functional analysis *in vivo*.

Another limitation stems from the sex differences in the karyotypes of the cell types used in this study. The iPSC-derived microglia used had a male karyotype, whereas the neurons and astrocytes derived from human neural stem cells (hNSCs) had a female karyotype[104]. These sex-specific differences may influence cellular responses and contribute to some of the observed outcomes. Future studies would benefit from a systematic examination of how sex-linked genetic and epigenetic differences and genetic variation affect RABV infection dynamics in human brain cell models.

Despite these limitations, our single-cell RNA-seq analysis using the Tha/Tha2P4M RABV study system in human brain cell-type co-cultures provides a powerful approach to discover key features of host-RABV interactions and a road map for building testable hypotheses regarding the dynamics and key molecular interactions that drive neurotropic infection in the brain.

Acknowledgements

We thank Anne Danckaert and Nathalie Aulner (UTechS Photonic BioImaging (PBI) core at Institute Pasteur Paris) for help with the image acquisition using the Opera Phenix Plus High Content Screening System (Perkin Elmer) and data analysis using the Columbus software (Perkin Elmer). PBI is a member of the national infrastructure France-BioImaging supported by the French National Research Agency (ANR-10-INBS-04). We acknowledge financial support of the Région Ile-de France (program DIM1Health, to H.B.), the Institut Pasteur (H.B. and L.F.), the Sloan Foundation (to A.S.) and the NIH Brain Initiative (R01 MH130464, to A.S.). We thank all other members of the Saunders and Bourhy's labs for helpful discussions of this work.

Author contributions

Conceptualization (LF, KY, HB, AS); Data Curation (ZG, JPC); Formal Analysis (KY, GC, LBA, AS); Funding acquisition (HB, AS); Investigation (LF, TK, LK); Methodology (LF, KY, AS); Project Administration (HB, AS); Resources (LF, VL, FG, MH); Software (ZG, AS); Supervision (HB, AS); Validation (LF, AS); Visualization (KY, GC, AS); Writing – original draft (LF, AS); Writing – review & editing (LF, KY, GC, HB, AS).

Declaration of interests

The authors declare no competing interests.

Figures

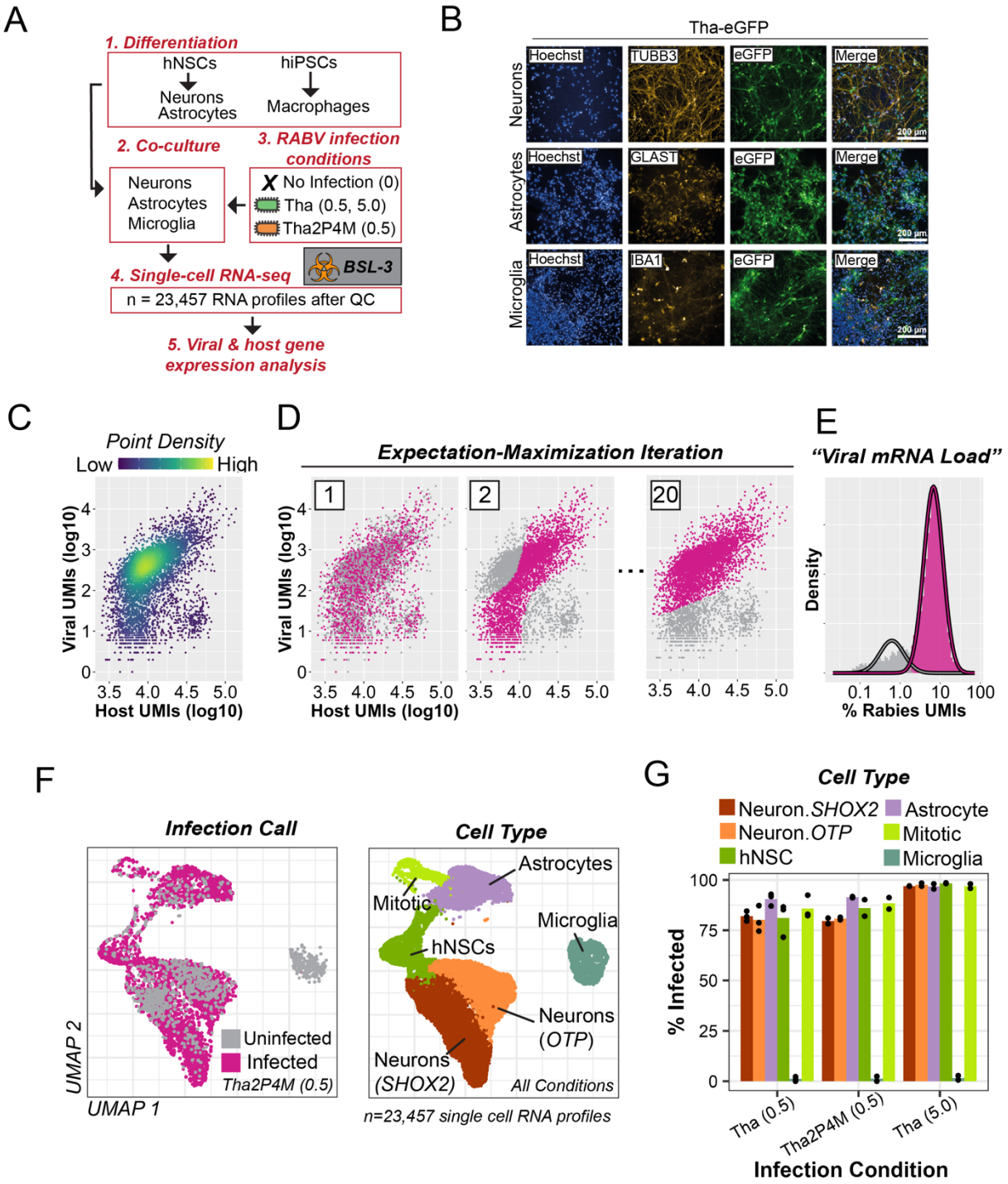

Figure 1. Unmasking the transcriptional effects of innate immune signaling inhibition across human brain cell types using field-isolate Tha wild-type and 2P4M RABV and single-cell RNA-seq analysis.

(A) Overview of the study system and scRNA-seq data generation. Human induced neural stem cells (hiNSCs) or pluripotent stem cells (hiPSCs) were transformed into neurons/astrocytes or macrophages and co-cultured, further inducing macrophage transformation into microglia. Under Biohazard Safety Level 3 conditions, scRNA-seq analysis was performed on acutely dissociated cells 48 hours after no viral infection (n=3 replicates) or bath application of Tha virus at MOI 5 (Tha(5); n= 2 replicates) or MOI 0.5 Tha(0.5); n= 3

replicates) and Tha2P4M virus at MOI 0.5 (Tha2P4M(0.5); n=2 replicates). After quality control, the final dataset consisted of 23,457 RNA profiles and included 23,528 human and 5 RABV genes.

(B) Immunolabeling of cell type marker proteins on co-cultured cells after infection of Tha RABV expressing eGFP (Tha-eGFP), confirming the presence of infected human-induced neurons (TUBB3), astrocytes (GLAST) and microglia (IBA1).

(**C-E**) Transcriptional identification of infected and uninfected cell types.

(C) Density plot comparing the number of viral UMIs versus total (viral + human) UMIs for each scRNA profile in the analysis.

(D) Systematic identification of infected and uninfected scRNA profiles using an Expectation-Maximization modeling approach to distinguish two cell populations based on viral UMIs (regressed by total UMIs)(**Methods**). Example results of infected (magenta) and uninfected (gray) scRNA profiles at iteration 1 (random assignment), iteration 2 and 20 (after convergence) are shown.

(E) Density plots of "viral mRNA load" (the percentage of total UMIs that are viral) for scRNA profiles called as infected (magenta) or uninfected (gray). (Infected, mean = 3.9±0.03 sem; range: 0.38 – 64.8; Bystander, mean = 0.17± 0.002 sem; range: 0-0.64).

(F) UMAP plot showing two dimensional embeddings of scRNA profiles following Seurat-based clustering analysis using exclusively human genes (**Methods**). scRNA profiles colored by infection status (*left*) or cell type-based cluster assignments (*right*).

(G) Barplots of the percent infected cells stratified by experimental condition and cell type.

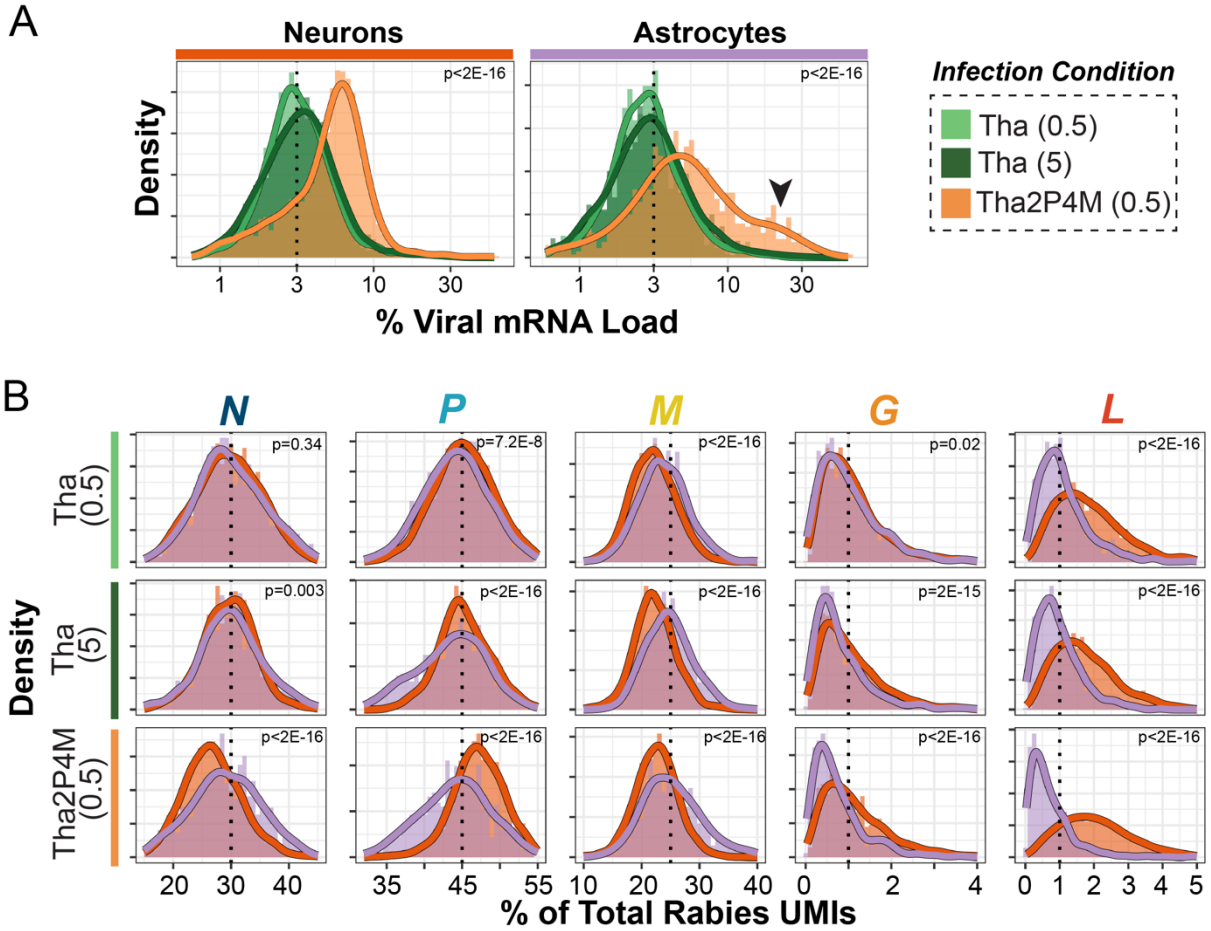

Figure 2. Tha2P4M mutations double viral mRNA load without major alterations to cell-type-specific viral gene expression.

(A) Combined density and histogram plots of viral mRNA load stratified by neurons and astrocytes and color-coded by experimental condition (n cells: Neurons, Tha(0.05) = 2,711; Tha(5) = 1,877; Tha2P4M(0.05) = 2,080; Astrocytes, Tha(0.05) = 1,036; Tha(5) = 798; Tha2P4M(0.05) = 806). Arrowhead indicates high viral mRNA load astrocytes. Both cell type and experimental condition explain differences in viral load distributions (p<2E-16, Kruskal-Wallis test).

(B) Combined density and histogram plots of relative RNA levels for each of the five Tha RABV genes color-coded by cell type and stratified by both gene identity and experimental condition. P values for differences in Neuron versus Astrocyte expression distributions are reported for each gene and experimental condition in the figure panel (Kolmogorov-Smirnov tests). (N mean %, Neurons: 26.8±0.11 sem; Astrocytes: 28.6±0.24; P mean %, Neurons: 47.3±0.08 sem; Astrocytes: 43.9±0.19; M mean %, Neurons: 22.6±0.08 sem; Astrocytes: 25.9±0.22; G mean %, Neurons: 1.19±0.02; Astrocytes: 0.79±0.03; Mean % *L* of viral RNA, Neurons: 1.9±0.01; Astrocytes: 0.99±0.02).

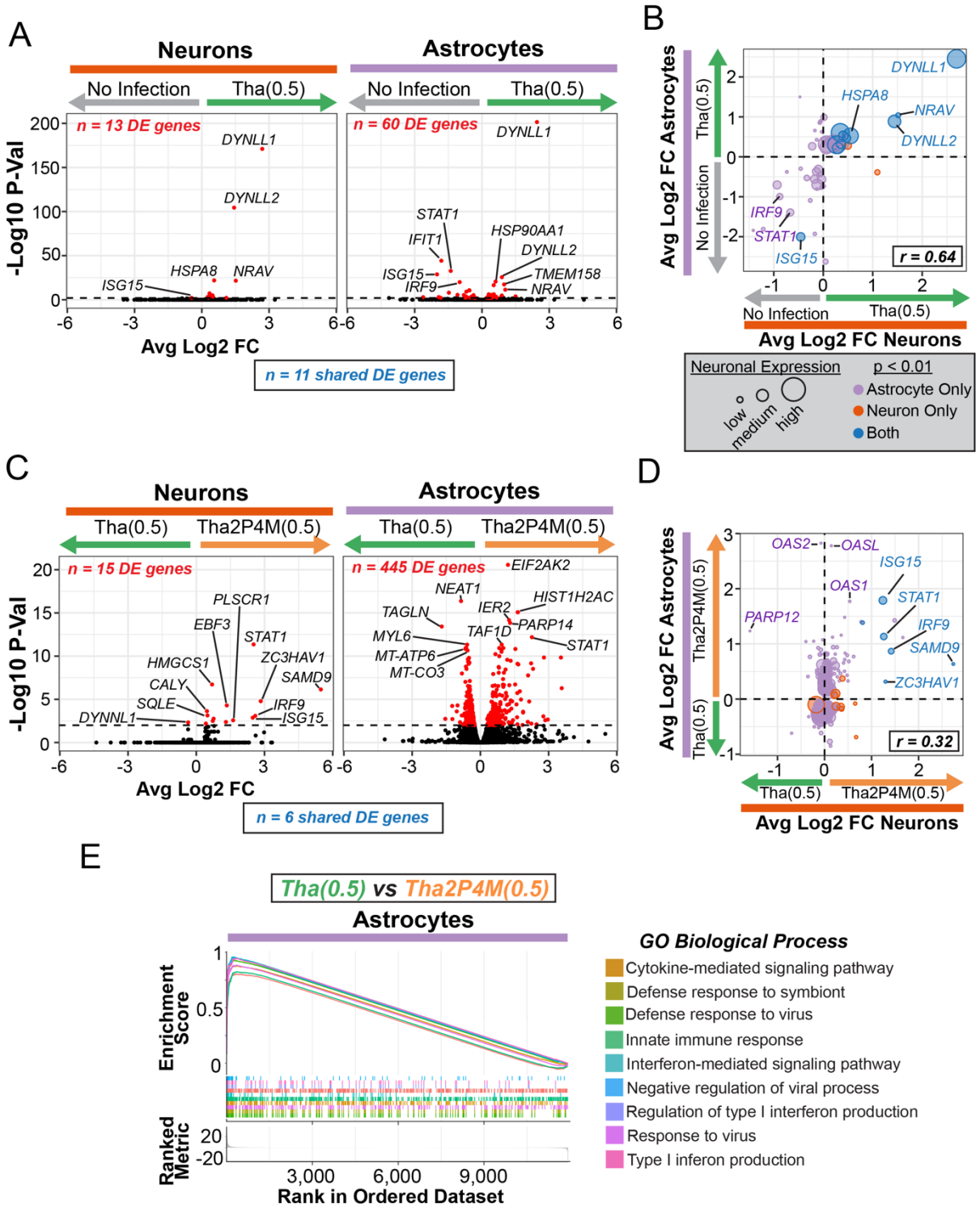

Figure 3. Tha2P4M mutations unmask a large-scale astrocyte-specific transcriptional response to infection.

(A-D) Genome-wide differential expression comparisons between neurons and astrocytes across No Infection and Tha(0.5) infected (**A,B**) or infected Tha(0.5) and infected Tha2P4M(0.5) experimental conditions (**B,C**). Arrow color and direction indicates higher levels of mRNAs in that experimental condition.

(A,C) Volcano plots of gene expression differences with select genes labelled (red, $p < 0.01$).

(B,D) Scatter plots comparing log2 fold expression level changes for genes significantly altered ($p < 0.01$) in either neurons (orange), astrocytes (purple) or both cell types (blue). Circle size is proportional to expression level in uninfected neurons.

(E) Gene set enrichment analysis of Biological Process Gene Ontology categories for differentially expressed genes ($p < 0.01$) across astrocytes infected with Tha(0.5) versus Tha2P4M(0.5) RABV. Gene set Enrichment Scores are shown for the nine most significantly enriched Biological Processes.

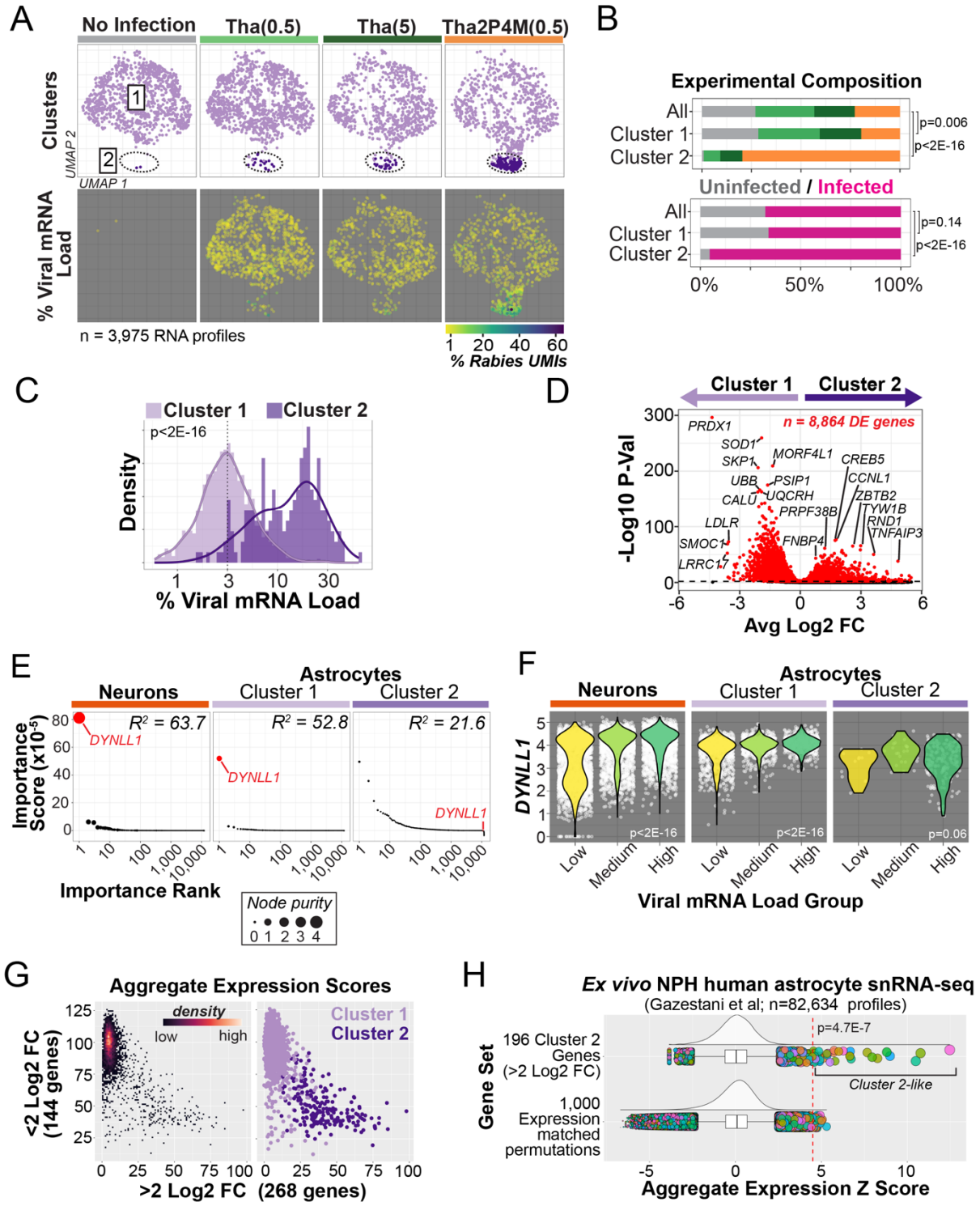

Figure 4. A pro-viral human astrocyte subpopulation supports high viral mRNA load and is decoupled from typical host cell transcriptional feedback through a massive alteration in RNA levels.

(A) UMAP embedding plot of astrocyte scRNA profiles clustered exclusively by human gene expression differences and stratified by experimental condition (**Methods**). "No infection" (grey) counts include scRNA profiles from cells that belonged to the non-infected control well where RABV infection was completely absent. *Top*, color-coded cluster identities. (Cluster 1, n=3,759 cells; Cluster 2, n=216 cells). *Bottom*, heat map of viral mRNA load scores.

(B) Bar plots comparing the composition single astrocyte RNA profiles from the full dataset versus Cluster 1 or Cluster based on experimental identity (Cluster 1 versus All: p=0.006; Chi-square test; Cluster 2 versus All: p<2.2E-16) or by infection status (Cluster 1 versus All: p=0.14; Cluster 2 versus All: p<2.2E-16). "Uninfected" counts include both uninfected "bystander" astrocytes and uninfected astrocytes from the "No Infection" condition.

(C) Combined histogram and density plot comparing viral mRNA load distributions for Cluster 1 and 2 (Mean viral load: Cluster 1, 2.2%±0.04 sem; Cluster 2, 13.8%±0.7; p < 2.2E-16, Kolmogorov-Smirnov test).

(D) Volcano plot of gene expression differences across Cluster 1 and 2 with select genes labelled (red, p < 0.01).

(E) Random forest regression analysis of n=11,943 human gene RNA levels predicting viral mRNA load stratified by neurons, Cluster 1 and Cluster 2 astrocytes. Genes are rank ordered by importance score and dot size indicates node purity (**Methods**). Goodness of fit for each model is reported (R^2).

(F) Violin plots of *DYNLL1* expression levels stratified by both cell type and viral mRNA load groups (Neurons, p<2E-16; Astrocytes Cluster 1, p<2E-16; Astrocytes Cluster 2, p=0.05. Kruskal-Wallis tests).

(G-I) Identification of rare "Cluster 2-like" astrocytes from single-nuclei RNA profiles derived from *ex vivo* cortical resections of living human Normal pressure hydrocephalus (NPH) surgical patients[79].

(G) Scatterplot of Cluster 1 or 2 astrocyte single-cell RNA profiles based on aggregate expression scores for genes up regulated in Cluster 1 (n=144 genes) or Cluster 2 (n=268 genes) (p < 0.01 and log2 fold-change > 2). *Left*, heat map of point densities. *Right*, color-coded cluster identities.

(H) Analysis of Cluster 2 aggregate gene scores for n=82,634 single-nucleus RNA profiles of astrocytes from n=52 NPH patients (median nuclei profile per patient = 1,277). Density and boxplots show aggregate expression z-score distribution for the 196 genes shared across both datasets (*top*) versus 1000 permutations of expression-matched NPH gene sets (**Methods**). snRNA-seq profiles > 4.5 standard deviations above the mean were considered "Cluster 2 like" (n=38 profiles identified in 21 of 52 total patients; p=4.7E-7 based on permutations). In box plots, outlier nuclei profiles (> 1.5 interquartile range) are shown as dots color-coded by patient identity and dot size proportional to the z-score.

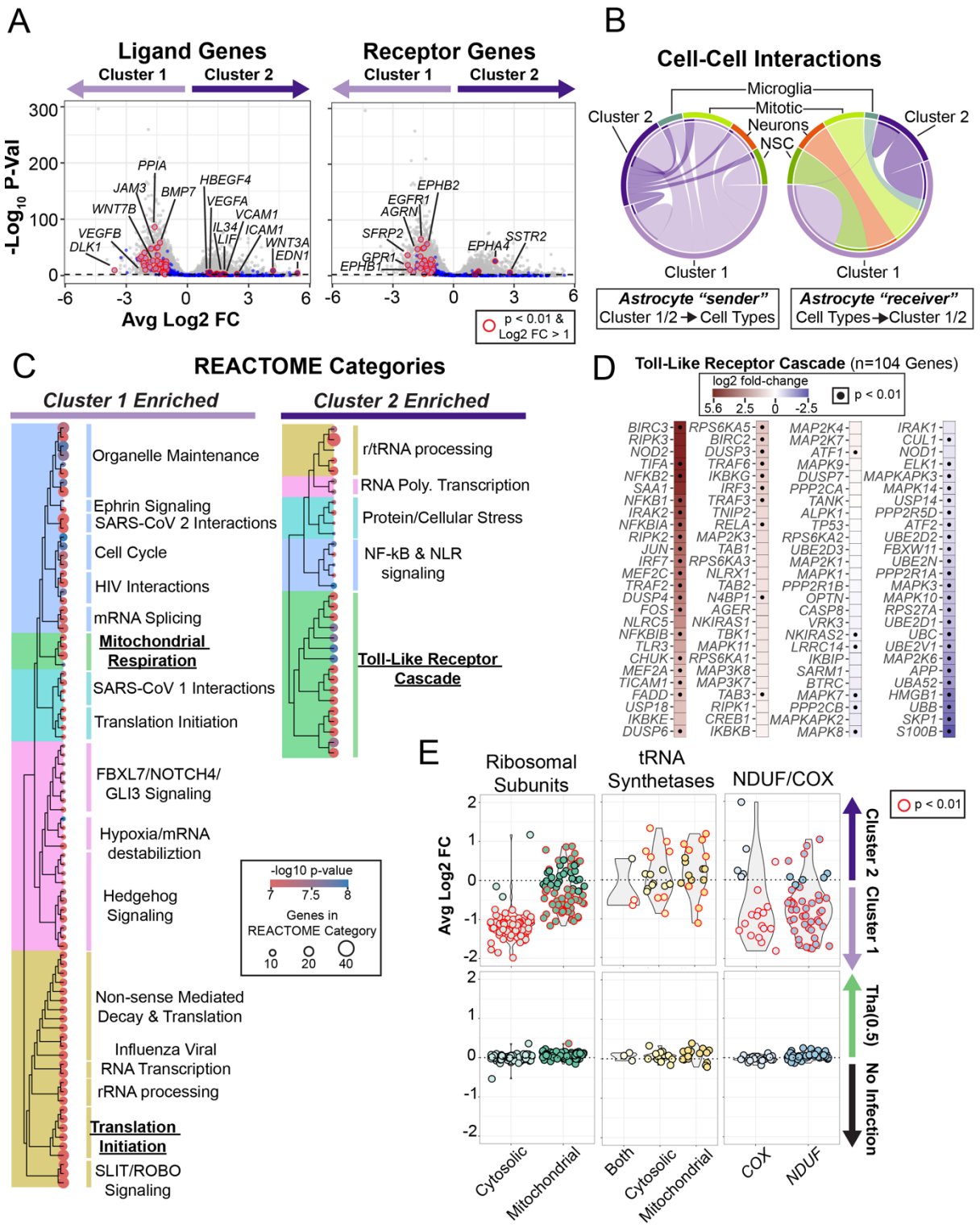

Figure 5. Gene expression changes in pro-viral human astrocytes imply reduced inter-cellular interactions, activation of toll-like receptors and complex changes in protein translation and mitochondrial respiration.

(A,B) Gene expression inference of alterations to inter-cell type interactions between Cluster 1 and Cluster 2 astrocytes using CellPhoneDB (CPDB) v5.0[105], a database of 1,419 molecular interactors (**Methods**).

(A) Volcano plot-based visualizations of ligand (*left*) or receptor (*right*) gene expression changes between Cluster 1 and Cluster 2. Ligand or receptor genes significantly enriched in either cluster ($p<0.01$) and significantly "relevant" (after CPDB permutation; $p < 0.05$) are circled in red (Ligand genes: Cluster 1, n=46; Cluster 2, n=11; Receptor genes: Cluster 1, n=32; Cluster 2, n=5). Other ligand or receptor genes are shown in blue and all other genes in gray.

(B) Chord diagrams showing the number of CPDB relevant interactions from (*left*) or to (*right*) Cluster 1 or Cluster 2 astrocytes for other cell types. The proportional size and color of the outer ring corresponds to the relative number of interactions by cell type. The color and proportion of the inner ring corresponds to interactions from or to Cluster 1 or Cluster 2 astrocytes.

(C) Tree plot clustering of enriched REACTOME gene categories (Cluster 1: $p < 0.000001$, n=84 categories; Cluster 2: $p < 0.01$, n=32 categories) based on genes upregulated in Cluster 1 (*left;* n=6,551) or Cluster 2 (*right;* n=2,347)($p<0.01$). Hierarchical clustering results reflect shared genes driving each REACTOME category association. Dot size scales with the gene number in each category. Heat map indicates p value of each included category. Underlined REACTOME categories are the focus of panels (**D**) and (**E**).

(D) Heat map plot reflecting log2 fold-changes in Cluster 2 of each gene in the Toll-Like Receptor Cascade REACTOME category (R-HSA-168898; n=104 genes). Dots indicate significant expression changes ($p < 0.01$).

(E) Combined violin and dot plots reflecting gene-specific log2 fold-changes for gene sets encoding proteins related to protein translation (*left* and *middle*) or mitochondrial respiratory complexes I and IV (*right*). *Top row*, Cluster 1 versus Cluster 2 astrocytes. *Bottom row,* No Infection versus Tha(0.5) RABV infected astrocytes. Ribosomal subunit genes are stratified by whether the encoded protein is a component of cytosolic (n=85 genes) or mitochondrial (n=78 genes) ribosomes. tRNA synthetase genes are stratified by whether the encoded enzyme aminoacyl-tRNAs used for translation in the cytosol (n=17 genes), mitochondria (n=17 genes) or both ribosome types (n=3 genes). Nuclear gene components or assembly factors of the cytochrome c oxidase (*COX*) family (n=23 genes), Complex IV. The NADH:ubiquinone oxidoreductase (*NDUF*) family (n=47 genes) encoding Complex I. Red outlines indicate significant expression changes ($p <0.01$).

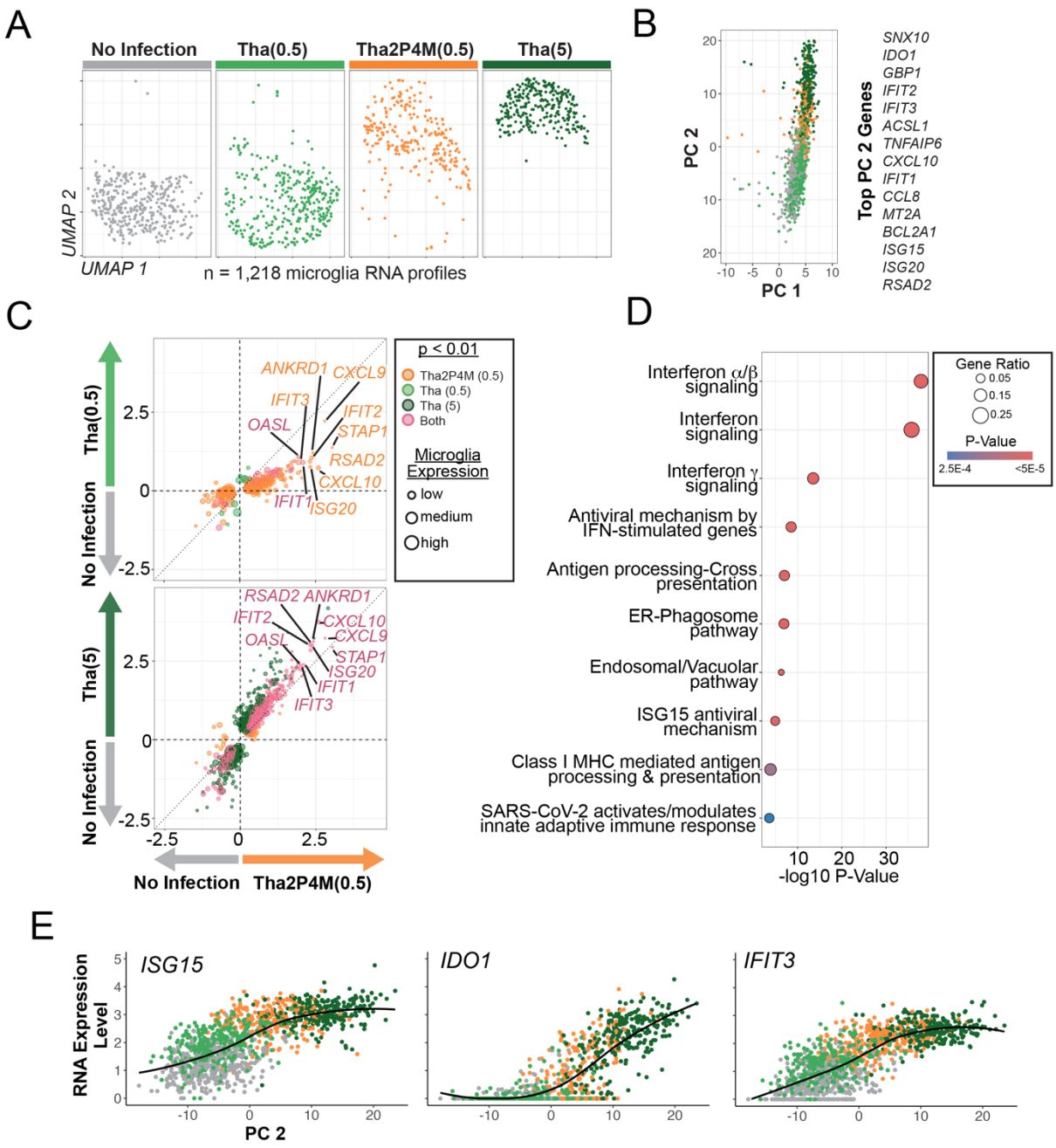

Figure 6. Uninfected microglia respond to Tha RABV infection through graded interferon stimulated gene transcription potentiated by higher viral titer and disinhibited innate immune signalling of other infected cell types.

(A) UMAP embedding plot of microglia scRNA profiles stratified by experimental condition (**Methods**)(n=1,218 cells).

(B) Principal component analysis of variably expressed microglia genes. *Left*, cell component loadings of PC 1 (contamination of neuronal RNAs; **Figure S8B**) versus PC 2 (interferon stimulated gene expression; **Figure S8B**). *Right*, n=15 genes with the highest gene loadings for PC 2.

(C). Scatter plots comparing log2 fold expression level changes of differentially expressed genes ($p < 0.01$) across No Infection microglia and microglia from various experimental conditions (*top*, Tha(0.5) versus Tha2P4M(0.5); *bottom*, Tha(5) versus Tha2P4M(0.5)). Color

reflects significant genes shared across comparisons (pink) versus those unique to experimental conditions. The dotted unity line (slope = 1, y intercept = 0) serves as a reference to indicate equivalent log2 fold changes across conditions.

(D) REACTOME pathway analysis plot based on n=202 shared genes found differentially expressed in comparisons of both Tha2P4M(0.5) and Tha(5) to No Infection microglia.

(E) Normalized gene expression plots for three representative interferon stimulated genes plotted against principal component 2 scores and color-coded by experimental condition.

Supplemental Figures

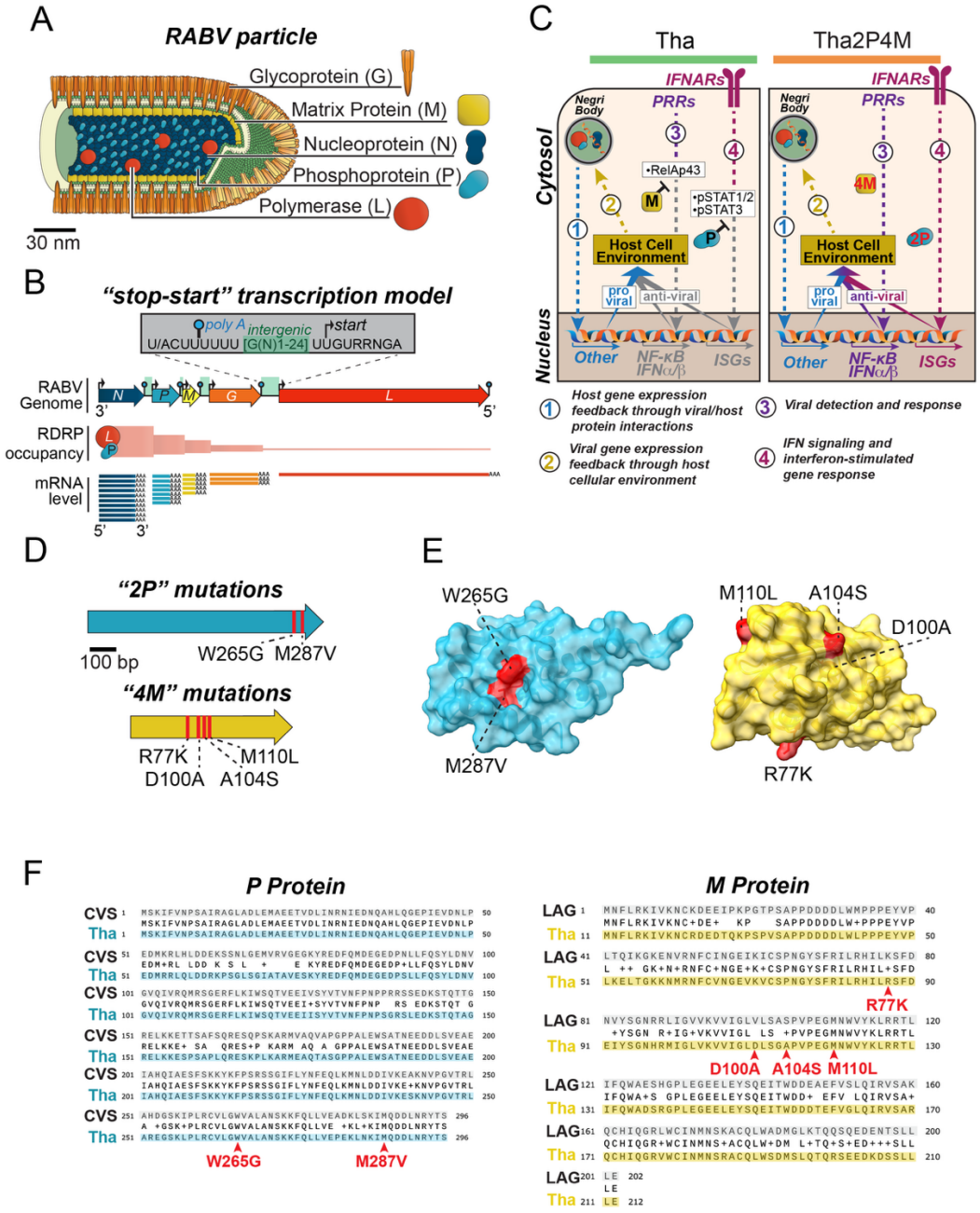

Supplemental Figure 1. "2P4M" mutations in Tha RABV P and M proteins disinhibit innate immune detection and responses in host cells by neutering negative regulation of NF-kb and IFN-stimulated gene transcriptional factors.

(A) Schematic illustrations of the RABV particle (modified from[2]).

(B) Schematic of the RABV genome and accepted "start-stop" model of transcription (after[2]). RABV genes are expressed at levels that reflect genome order due to the occupancy of the RNA-dependent RNA Polymerase (RNDP) complex composed of the polymerase (L) and co-factor P. RNA sequence motifs responsible for the stop/polyadenylation ("poly A") and transcriptional onset ("start") functions of the RNDP are shown.

(C) Schematic illustrating known mechanisms of RABV P and M inhibition of viral detection and response in Tha (*left*) or Tha2P4M (*right*) infection along with basic pathways (numbered below) through which viral/host interactions and inhibited/disinhibited innate immune signaling could affect viral and host cellular processes. Germline-encoded pattern recognition receptors (PRRs) are viral sensors (such as toll-like receptors (TLRs); retinoic acid-inducible gene I (RIG-I) like helicases (RLRs); and nucleotide-binding oligomerization domain-like receptors (NOD-like receptors) that induce NF-kB and IFN pathways upon activation.

(D) Gene locations and amino acid alterations of six key point mutations that restrict innate immune inhibition by P ("2P") and M ("4M") proteins.

(E) Protein structures of lyssavirus P (RABV CVS strain[106]) and M (Lagos bat virus[107]) highlight the outward-facing locations of mutant residues in P and M (red). P mutations cluster around the "W hole" (after[34]); M mutations affect three spatially-distinct interaction sites.

(F) Amino acid-based protein alignments comparing Tha RABV P and M proteins versus those protein sequences from the solved structures shown in (**E**)(CVS P[106] (PDB Accession 1vyi) and Lagos Bat M[107] (PDB Accession 2w2s). The sites of the "2P" and "4M" mutations are shown in red.

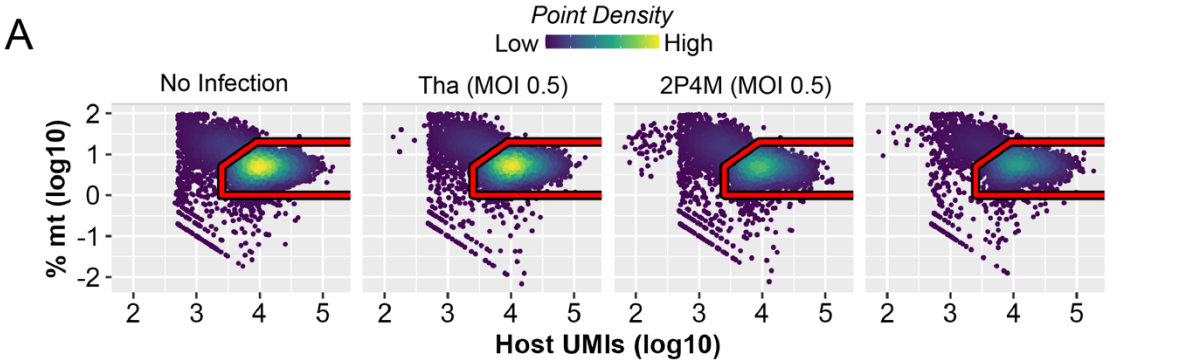

B

Condition	No Infection			Tha (MOI 0.5)			Tha2P4M (MOI 0.5)		Tha (MOI 5)		Total
Experimental Replicates	1	2	3	1	2	3	1	2	1	2	10
Passing Cells	2,825	2,201	2,298	2,321	2,405	2,300	2,593	2,471	1,934	2,109	23,457

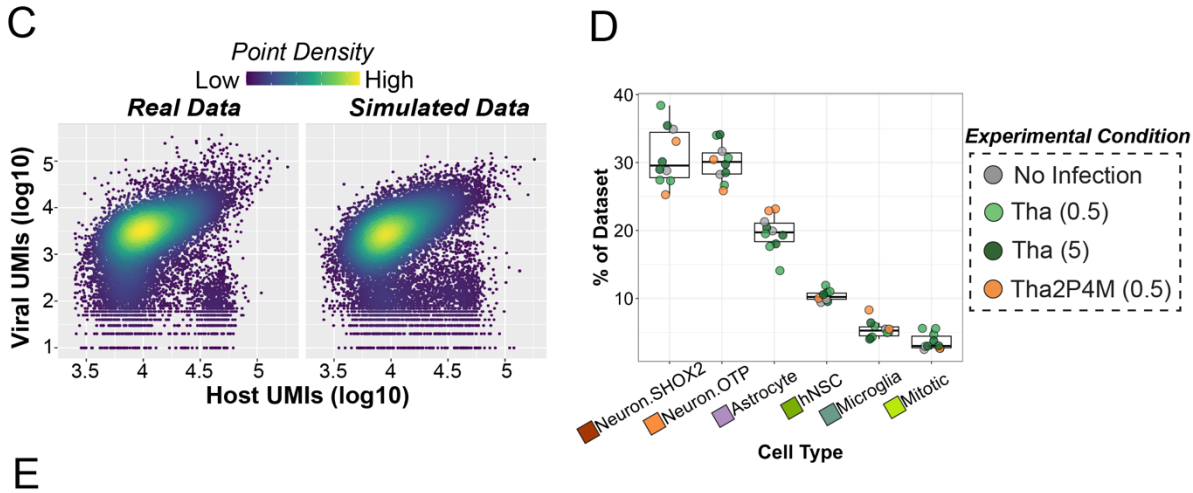

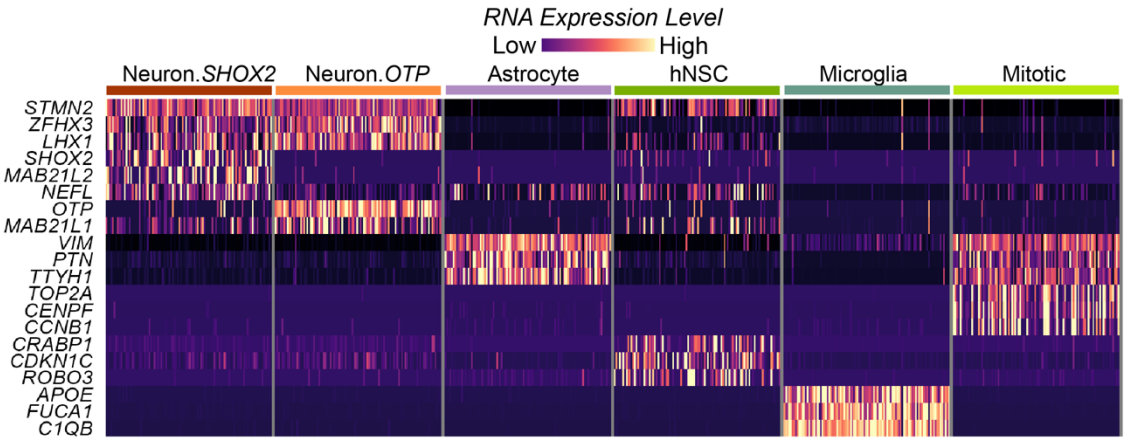

Supplemental Figure 2. Quality-control metrics for scRNA-seq analysis and expectation-maximization approach for distinguishing RABV infected and uninfected bystander cells from human brain co-cultures.

(A) Quality-control metrics for inclusion of scRNA profiles. Density scatter plots compare the size of RNA libraries (based on total human UMI counts) versus the fraction of RNA derived from the mitochondrial genome. The red polygons define high-quality RNA libraries included for downstream analysis. Colored heat map indicates point density.

(B) Table summarizing the number of RNA profiles for each replicate across experimental conditions.

(**C**) Density plot-based comparison of the real versus simulated data of viral versus total UMI counts, demonstrating the accuracy of the model used for Expectation-Maximization identification of RABV infected versus uninfected cells (**Methods**).

(**D**) Box plot of cell type percentages across scRNA-seq datasets. Replicate-specific cell type percentages are shown with dots color-coded by experimental condition.

(E) Heat map depiction of expression levels of select marker genes for transcriptional clusters associated with major human brain cell types. Colored heat map indicates expression level. Cells are downsampled by cell type for visualization.

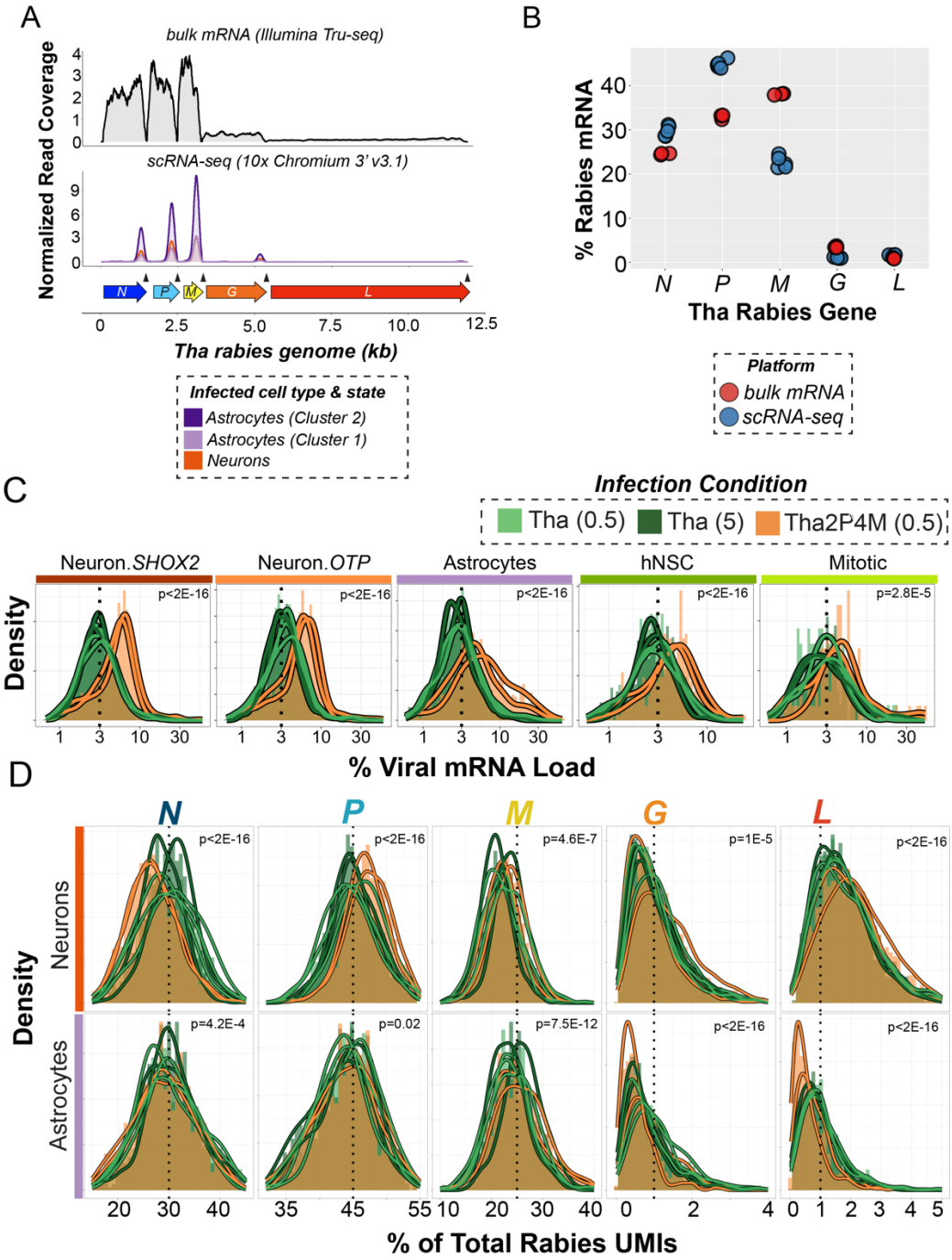

Supplemental Figure 3. RNA expression analysis of Tha RABV genes

(A) Comparison of normalized sequencing read coverage across the Tha RABV genome for bulk RNA sequencing (*top*) following poly A capture and enrichment[35] versus subsets of n=10 scRNA-profiles associated with Neurons and Cluster 1 and Cluster 2 Astrocytes (*bottom*)(**Figure 4A**; **Methods**). A schematic of the Tha RABV genome is shown at bottom and the locations of polyadenylation signals are indicated with arrow heads.

(B) Comparison of relative expression levels for each Tha RABV gene based on bulk RNA sequencing (red; three biological replicates) versus the scRNA-seq analysis used in this study (blue; five total biological replicates, n=3 Tha(0.5) and n=2 Tha(5) aggregated across all cell types). Range mean % viral mRNA, bulk: *N* = 24.3-24.6, *P* = 32-33, *M* = 38-38.2, *G* = 3.3-3.7, *L* = 0.8-1.0, scRNA: *N* = 29-31, *P* = 44-46, *M* = 21-22, *G* = 0.9-1.2, *L* = 1.1-1.2.

(C) Combined histogram and density plots of viral mRNA load stratified by brain cell types and color-coded by experimental replicate. P values reporting differences in distributions by experimental condition are reported in each panel (Kruskal-Wallis tests).

(D) Density plots of relative RNA levels for each of the five Tha RABV genes color-coded by experimental replicate and stratified by both gene and neuron (*top*) or astrocyte (*bottom*) identity. P values reporting differences in gene expression distributions by experimental condition are reported for neurons and astrocytes in each panel (Kruskal-Wallis tests).

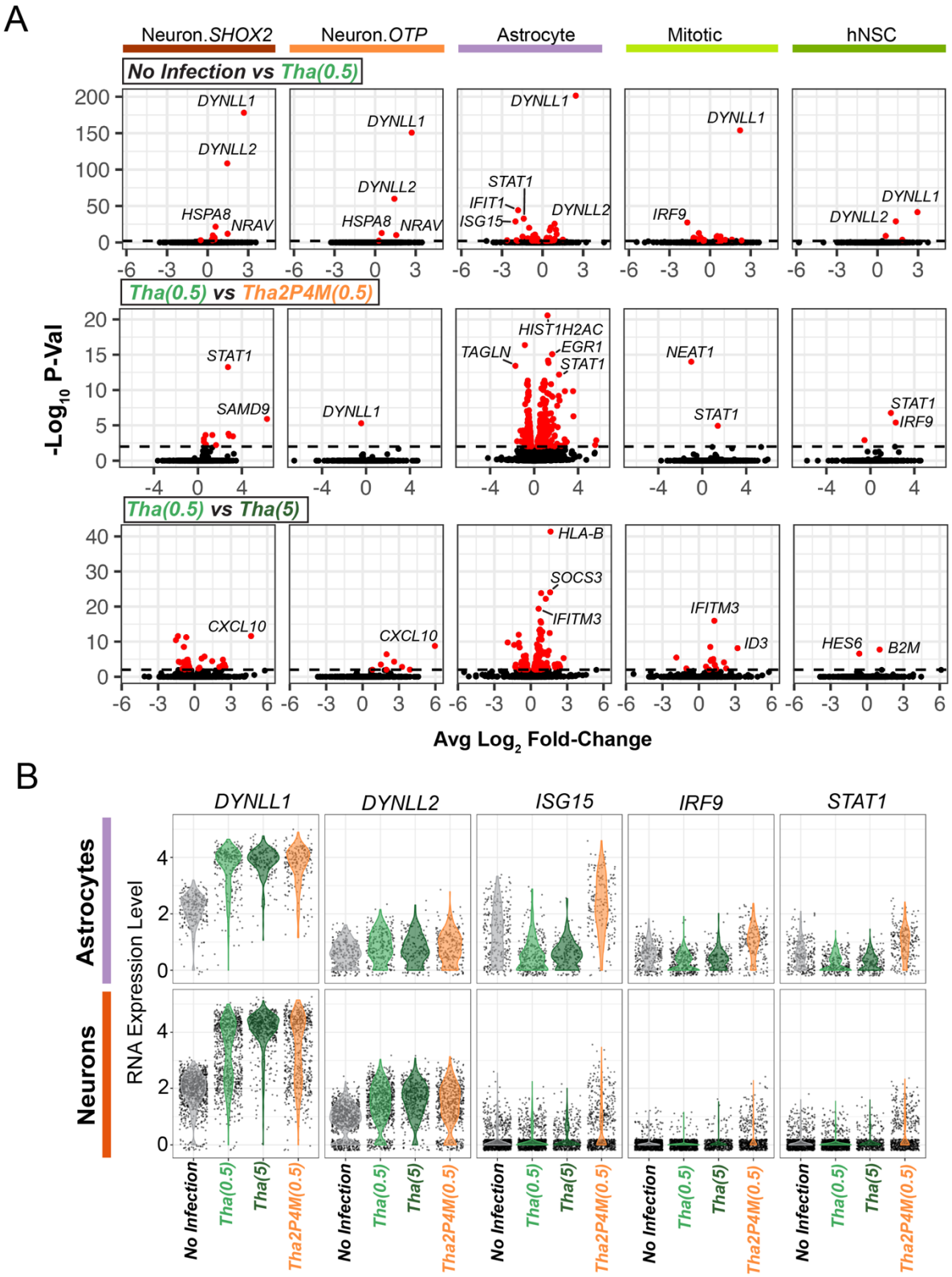

Supplemental Figure 4. Host cell gene expression responses to different RABV infection conditions.

(A) Volcano plots of genome-wide expression differences stratified by cell type and experimental condition (*top row*, No Infection versus Tha(0.5); *middle row*, Tha(0.5) versus Tha2P-4M(0.5); *bottom row*, Tha(0.5) versus Tha(5)). Select genes with significant differences (red, $p < 0.01$) are labelled for clarity.

(B) Combined violin dot plots stratified by astrocytes (*top*) or neurons (*bottom*) illustrating RNA expression levels for key genes stratified by experimental condition. (RNA levels are shown as after log-normalization and centering following the default Seurat workflow; **Methods**).

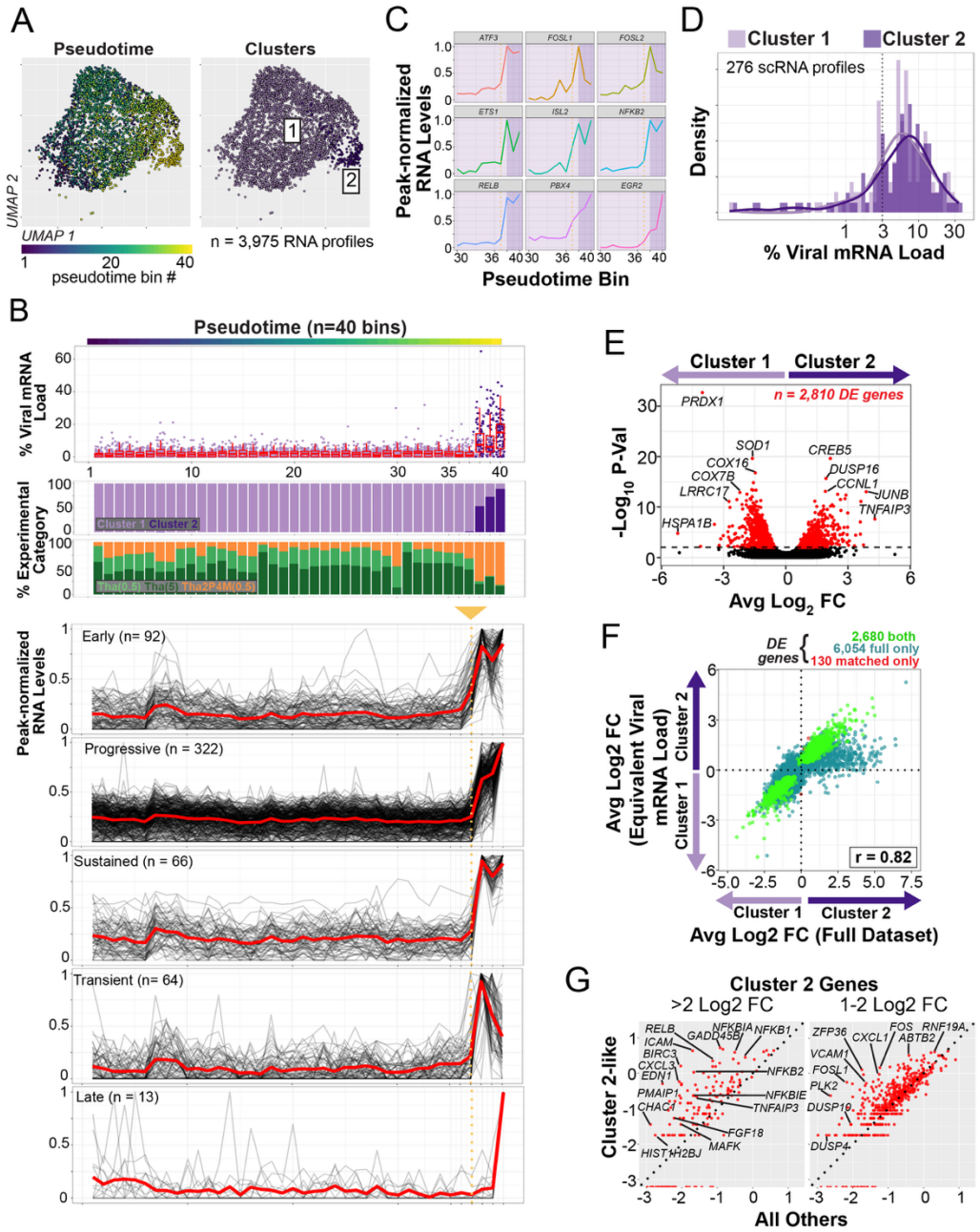

Supplemental Figure 5. Large-scale gene expression changes driving pro-viral Cluster 2 astrocyte identities precede and are largely independent of viral mRNA load.

(A-C) Pseudotime trajectory analysis of astrocyte scRNA profiles performed using Monocle3 **(Methods).**

(A) UMAP embeddings of astrocytes. *Left*, after binning into n=40 pseudotime groups and color-coded by a heat map. *Right,* Cluster 1 and Cluster 2 identities from the Seurat-based clustering analysis (**Figure 4A**).

(B) Linear plots of astrocyte experimental or expression properties ordered by psuedotime bin. *Top*, viral mRNA load scores of each astrocyte (dots) color-coded by cluster identity along with bin-specific box plots (red). *Middle*, bar plots displaying the proportion of astrocytes by cluster or experimental condition. *Bottom*, line plots of peak-normalized gene-specific expression signatures across pseudotime bins stratified by temporal expression pattern (black). Mean expression values across all genes in each category are shown in red. Dotted gold line and

1407 arrow mark the bin (number 37) preceding the increase in viral mRNA load and pro-viral Cluster
1408 2 identities. “Early” genes exhibit clear increases in expression that precede bin 37 in
1409 pseudotime (**Methods**). “Progressive”, “Sustained”, “Transient” and “Late” categories describe
1410 distinct expression signatures between bin 38 and 40 (**Methods**).

1411 **(C)** Peak-normalized expression signatures for n=12 transcription factors, selected as
1412 examples from the n=24 “early” genes identified as transcriptional regulators (belonging to the
1413 “chromatin” (GO:0000785) “cell component” Gene Ontology category (*ATF3, CENPA, CREB5,*
1414 *CSRNP1, EGR2, ETS1, FOSL1, FOSL2, FOXS1, HEY2, IRF1, ISL2, JADE1, JUNB, KLF5, MAFF,*
1415 *MEF2C, NFATC2, NFKB2, PBX4, RELB, TEAD4*). “Chromatin” genes were two-fold enriched in the
1416 “early” gene set (n=22 of 92; 24%) as compared to genes across all other categories in (**A**)
1417 (n=86 of 688; 12.5%)(p = 0.0008, Chi Square Test). Line plots for each gene are named and
1418 color-coded. Only pseudotime bins 30-40 are shown to highlight the Cluster 1 to Cluster 2
1419 transition. The dark purple background highlights bins 38-40 in which pro-viral astrocytes
1420 emerge (**B**).

1421 **(D)** Combined histogram and density plot of viral mRNA load distributions for Cluster 1 and 2
1422 after downsampling each cluster to n=276 scRNA profiles with equivalent viral mRNA load
1423 distributions (**Methods**).

1424 **(E)** Volcano plots of gene expression differences across viral mRNA load downsampled
1425 Cluster 1 and 2 with select genes labelled (red, $p < 0.01$).

1426 **(F)** Scatter plots comparing log2 fold expression level changes for genes significantly altered
1427 ($p < 0.01$) across Cluster 1 or Cluster 2 in the full dataset or a dataset in which viral mRNA
1428 load scores were downsampled to an equivalent distribution in Cluster 1 and 2 (**Methods**).
1429 Differentially expressed genes are color-coded by membership (shared, green; full dataset
1430 only, cyan; equivalent viral load only, red).

1431 **(G)** Scatterplots of normalized metacell expression values for the 196 genes used to identify
1432 “Cluster 2-like” profiles (Identification Gene Set: $p < 0.01$ and >2 log fold-change; *left*) and for
1433 an independent set of n=521 gene RNAs with enriched expression in Cluster 2 astrocytes
1434 (Validation Gene Set: $p < 0.01$ and 1-2 log fold-change; *right*)(**Methods**). Metacells are
1435 composed of n=38 “Cluster 2-like” nuclei RNA profiles versus all other astrocyte nuclei profiles
1436 in the NPH dataset (“All Others”; n=82,596). Total UMI counts for both NPH gene sets were
1437 significantly enriched in “Cluster 2-like” NPH astrocyte profiles at levels that matched
1438 expectation from Cluster 2 (Identification Gene Set, 2.8 fold enriched; Validation Gene Set, 1.2
1439 fold enriched; $p<2.2E-16$, Chi Square Test).
1440

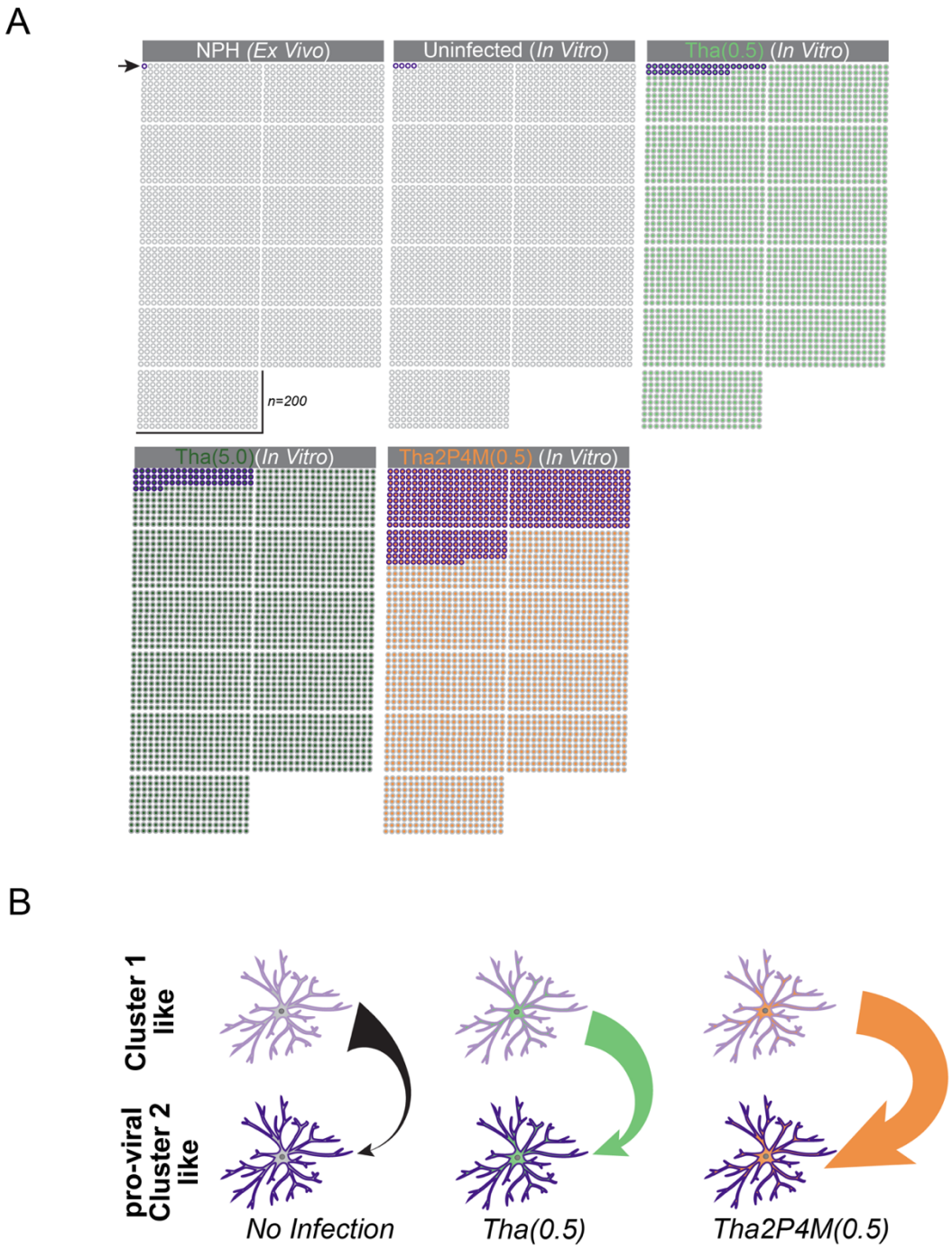

Supplemental Figure 6. Schematic of abundances and working model of pro-viral astrocyte state transition.

(A) Schematic approximating the abundance of astrocytes in the Cluster 2 (or Cluster 2-like) pro-viral state across experimental conditions estimated from the NPH and Tha datasets. Circles representing 2,200 astrocytes are shown. The experimental state is indicated by the dot fill, while the Cluster 2/Cluster 2-like state is indicated by a purple outline (beginning at top left, as indicated by the arrow).

(B) Cartoon model illustrating the relative abundances and Cluster 1-like or pro-viral Cluster 2 like astrocytes in different RABV conditions. Arrowhead and tail width indicate the relative proportion of each astrocyte state, with larger widths indicating higher proportions. Without infection, pro-viral Cluster 2 like astrocytes are present, but rare. RABV infection increases the

likelihood of Cluster 1-like astrocytes transitioning to a pro-viral like state. When the 2P4M mutations are present, the likelihood of this transition is much higher. It is unknown whether pro-viral astrocytes can transition back to a more Cluster 1 like state.

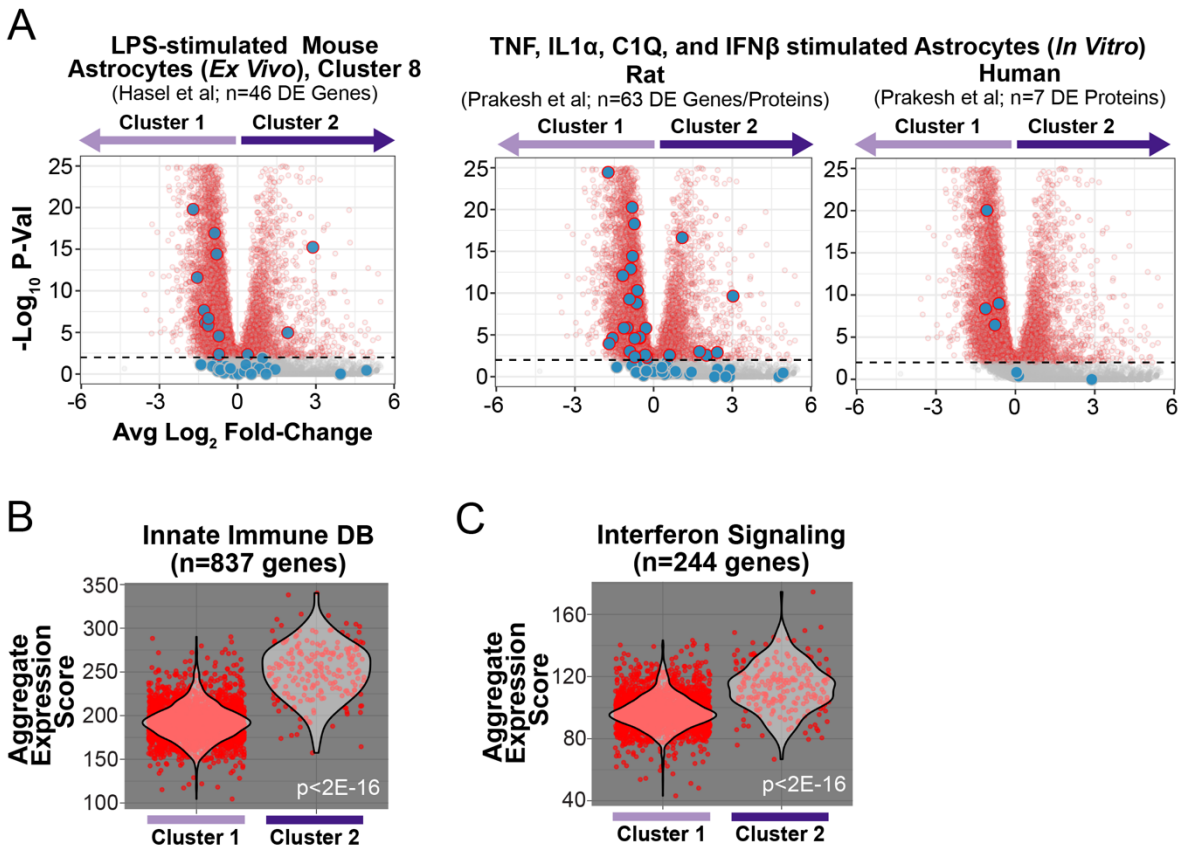

Supplemental Figure 7. Gene expression signatures observed in pro-viral Cluster 2 astrocytes are not observed in previous descriptions of "reactive" rodent or human astrocytes.

(A) Plots of differentially expressed RNAs or proteins from previous studies plotted on volcano plot of depicting expression differences across Cluster 1 and Cluster 2 astrocytes. The size and color of dots represents the intersection of differentially expressed RNAs or proteins from previous studies with those RNAs differentially expressed across Cluster 1 or Cluster 2. Large blue dots correspond to previously described as differentially expressed gene/protein sets ($p < 0.01$); those with red outlines are also significant in the Cluster 1 versus Cluster 2 comparison ($p < 0.01$). Smaller dots correspond to those genes observed as differentially expressed across Cluster 1 and Cluster 2 (red, $p < 0.01$; grey, $p >= 0.01$) but are not observed as differentially expressed in previous studies. *Left*, 46 genes differentially expressed following scRNA-seq analysis of mouse cortical astrocytes *ex vivo* with an IFN activated gene signature following Lipopolysaccharides (LPS) stimulation[81] . Primary rat (*middle*) or iPSC-derived human (*right*) astrocytes cultured *in vitro* and stimulated with TNF, IL1α, C1Q and IFNβ to induce an interferon-responsive state[80] . The 63 rat genes show concordant changes from bulk RNA-seq and proteomic analysis; the 7 human genes identify alterations based on proteomic analysis of secreted proteins (bulk RNA-seq was not performed).

(**B,C**) Aggregate expression scores across Cluster 1 and pro-viral Cluster 2 astrocytes for those n=837 genes annotated in the InnateImmuneDB database[82] (**B**) and n=244 human genes annotated in the "Interferon Signalling" REACTOME database category (R-HSA-913531)(**C**)(Wilcoxon Test).

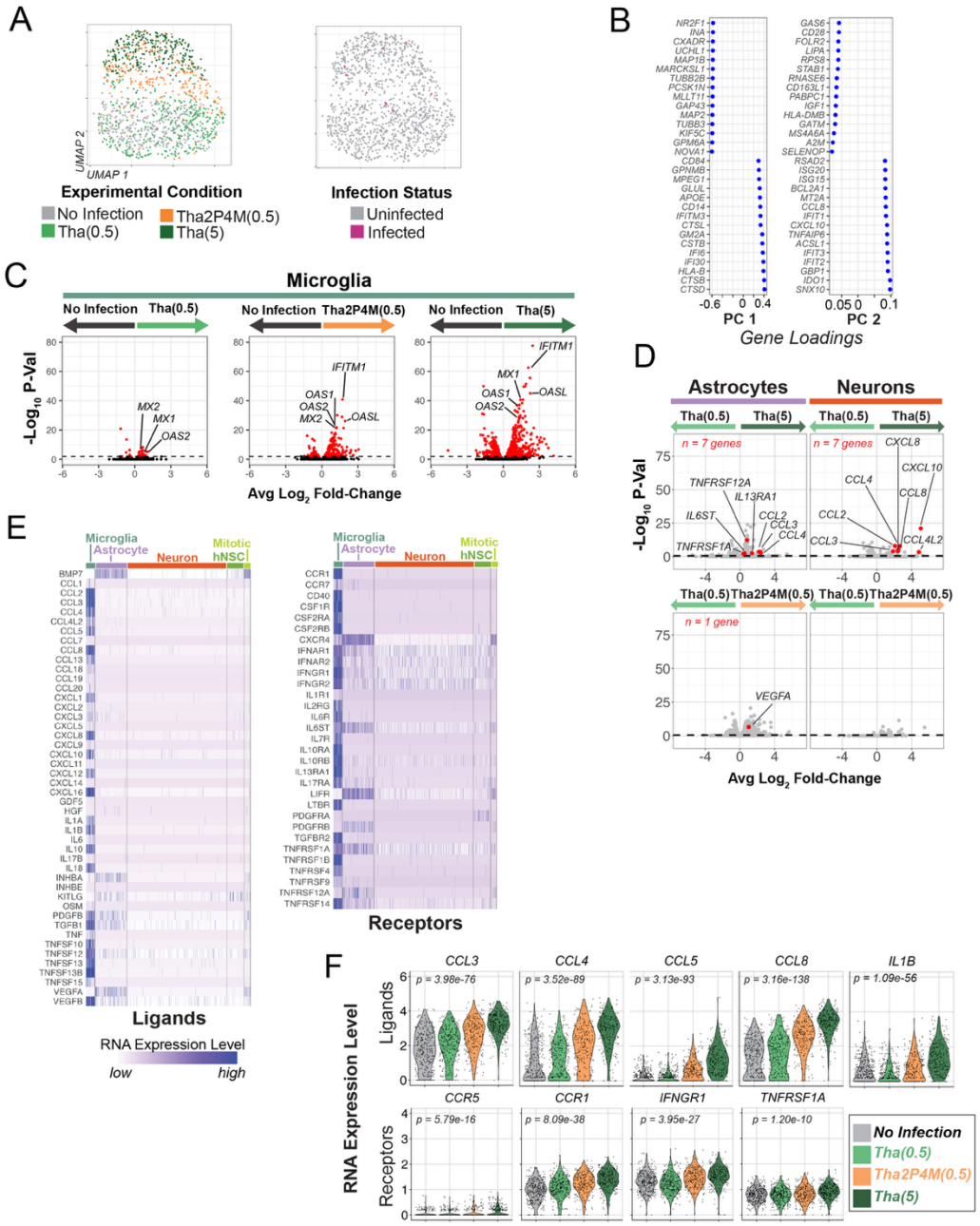

Supplemental Figure 8. Microglia transcriptional response to Tha RABV infection of other cell types.

(A) UMAP embedding plot of microglia scRNA profiles color-coded by experimental condition (*left*) and infection status (*right*).

(B) Gene principal component loading scores for the top and bottom n=15 genes for PC 1 and PC 2. PC 1 genes suggest contamination of neuronal transcripts, while PC 2 genes represent genes transcriptionally regulated by interferon signalling.

(C) Volcano plots of gene expression differences with select genes labelled (red, $p < 0.01$). The corresponding fold-change values for these analyses are shown in **Figure 6C**.

(**D**) Volcano plots displaying gene expression differences across experimental conditions for astrocytes and neurons (*top*, Tha(0.5) vs. Tha(5)(*top*); *bottom*, Tha(0.5) vs. Tha2P4M(0.5)).

1540 KEGG cytokine-cytokine receptor interaction pathway (M9809) genes with ($p < 0.01$) are
1541 shown in red. All other genes in grey.
1542
1543 (**E**) Gene expression heatmap of all cytokine ligand and receptor genes (KEGG cytokine-
1544 cytokine receptor interaction pathway M9809) (ligands, *left*; receptors, *right*) across cell types
1545 including all experimental conditions.
1546
1547 (**F**) Violin plots of microglia expression across experimental conditions for select cytokine
1548 ligands (*top*) and receptors (*bottom*) with known roles in NF-κB signalling (effect of
1549 experimental condition assessed with a one-way ANOVA, $\alpha < 0.01$). Example ligands and
1550 receptors show graded expression levels that are similar to microglia ISGs across
1551 experimental conditions (**Figure 6E**).
1552
1553

1554 Supplemental Table

1555 **Supplemental Table S1** contains all differential gene expression testing results reported in
1556 the manuscript.
1557

1558 Supplemental information

1559 STAR Methods

1560 KEY RESOURCES TABLE

REAGENT or RESOURCE	SOURCE	IDENTIFIER
Antibodies		
Mouse anti-TUBB3	Sigma	Cat# T858
Rabbit anti-GLAST	Invitrogen	Cat# PA5-111080
Rabbit anti-IBA1	Proteintech	Cat# 10904-1-AP
Goat Anti-mouse DYLIGHT 549	KPL	Cat# 072-04-18-06
Goat anti-rabbit Alexa Fluor 549	Invitrogen	Cat# A11035
Virus strains		
Tha RABV (8743THA)	Delmas et al.[108]	GenBank No. EU293121
Tha-eGFP RABV (based on 8743THA)	Besson et al. [109]	Ref-SKU: 014V-03195
Tha2P4M RABV (based on 8743THA)	Sonthonnax et al.[20]	N/A
Chemicals, peptides, and recombinant proteins		
Ascorbid acid	Sigma-Aldrich	Cat# A4403
BMP-4	R&D Systems	Cat# 314-BP-050
B-27 serum free supplement	Thermo Fisher	Cat#17504044
CHIR99021	TOCRIS	Cat# 4423
CSF-1	R&D Systems	Cat# 216-MC-01M
Dead Cell Removal Kit	Miltenyi Biotec	Cat# 130-090-101
DKK-1	R&D Systems	Cat# 5439-DK-500
EGF	Thermo Fisher	Cat# PHG0311
fetal bovine serum (heat inactivated)	Eurobio	Cat# S182H-500
FGF	Thermo Fisher	Cat# PHG0026
FGF-2	R&D Systems	Cat# 223-FB-500
Geltrex	Invitrogen	Cat# A1413201
Glutamax	Thermo Fisher	Cat# 35050038
Hoescht 33342	Thermo Fisher	Cat# H1399
IL-3	R&D Systems	Cat# 203-IL-050

IL-6	R&D Systems	Cat# 206-IL-050
IL-34	R&D Systems	Cat# 5265-IL-010
Knock-out D-MEM/F-12	Thermo Fisher	Cat# A1370801
Laminin	Sigma-Aldrich	Cat# L2020
Neurobasal medium	Thermo Fisher	Cat# 10888022
Papain	Sigma-Aldrich	Cat# P4762
PBS	Thermo Scientific	Cat# 10010023
Penicillin/Streptomycin	Thermo Fisher	Cat# 15140148
Poly-ornithine	Sigma-Aldrich	Cat# P4957
ROCK inhibitor Y-27632	Stemcell Technologies	Cat# ACS-3030
SCF	R&D Systems	Cat# 255-SC-01M
StemPro Accutase	Thermo Scientific	Cat# A1110501
StemPro Neural Supplement	Thermo Fisher	Cat# A1050801
Triton-X	Millipore	Cat# 648463
VEGF	R&D Systems	Cat# 293-VE-500

Critical commercial assays

Chromium Next GEM Single Cell 3' Kit v3.1	10x Genomics	Cat#: 1000121
Single Index Kit T Set A, 96 rxn	10x Genomics	Cat#: PN-2000240
NovaSeq 6000 S4 Reagent Kit v1.5 (300 cycles)	Illumina	Cat#: 20028312

Deposited data

scRNA-seq data (raw)	This paper	GEO: GSE284262
scRNA-seq data (processed)	This paper	https://drive.google.com/drive/folders/1Qnv4TorlnZ5z_Z6yzBMwJAIleGyXP9x9?usp=drive_link
Tha bulk mRNA seq data (raw)	Kim et al.	GEO: GSE178583
NPH snRNA sequencing data (processed)	Gazestani et al.	https://zenodo.org/records/8319719
Mouse astrocyte scRNA-seq (processed)	Hasel et al.	PMID: 34413515 (Supp. Table 5)
Rat astrocyte RNA-seq/proteomics (processed)	Prakash et al.	PMID: 8031883 (Supp. Table 5)
Human astrocyte proteomics (processed)	Prakash et al.	PMID: 8031883 (Supp. Table 5)

Experimental models: Cell lines

Human neural stem cells (EnStem-A™)	Millipore	Cat#: SCC003
XCL-1 iPSC	XCell Science	Cat#: IP-001-1V

Software and algorithms

R programming language (v4.3.0)	N/A	https://cran.r-project.org/
Python programming language (v3.8.19)	N/A	https://www.python.org/
STAR (v2.7.9a)	Dobin et al.[110]	https://github.com/alexdobin/STAR
RSEM (v1.3.1)	Li et al.[111]	https://github.com/deweylab/RSEM
CellRanger (v5.0.1)	10x Genomics	https://github.com/10XGenomics/cellranger
Seurat (v4.4.0)	Hao et al.[112]	https://cran.r-project.org/
tidyverse (v2.0.0)	Wickham et al.[113]	https://cran.r-project.org/
dplyr (v1.1.4)	Wickham et al.[114]	https://cran.r-project.org/
ggplot2 (v3.5.1)	Wickham[115]	https://cran.r-project.org/

Matrix (v1.6-4)	N/A	https://cran.r-project.org/
viridis (v0.6.5)	N/A	https://cran.r-project.org/
Libra (v1.0.0)	N/A	https://github.com/neurorestore/Libra
clusterProfiler (v4.8.3)	Xu et al.[116]	https://bioconductor.org/
enrichplot (v1.2.3)	Yu[117]	https://bioconductor.org/
ReactomePA (v1.44.0)	Yu et al.[118]	https://bioconductor.org/
ggrepel (v0.9.5)	Slowikowski[119]	https://cran.r-project.org/
ggtree (v3.8.2)	Yu et al.[120]	https://cran.r-project.org/
smplot2 (v0.2.4)	Min et al.[121]	https://bioconductor.org/
qs (v0.26.3)	N/A	https://cran.r-project.org/
data.table (v1.15.4)	Barrett et al.[122]	https://cran.r-project.org/
cowplot(v.1.1.3)	N/A	https://cran.r-project.org/
CellPhoneDB (v5.0)	Troulé et al.[105]	
circlize (v0.4.16)	Gu et al.[123]	https://cran.r-project.org/
PupillometryR (v0.0.5)	Forbes et al.[124]	https://cran.r-project.org/
Snapgene (v7.2.1)	Dotmatics	www.snapgene.com
monocle3 (v1.3.7)	Cao et al.[125]	https://github.com/cole-trapnell-lab/monocle3
randomForest (v4.7-1.2)	N/A	https://cran.r-project.org/

RESOURCE AVAILABILITY

Lead contact

Further information and viral reagent requests will be fulfilled by lead contacts Dr. Arpiar Saunders and Dr. Hervé Bourhy.

Materials availability

Tha RABV reagents are available from Dr. Hervé Bourhy with a completed MTA and appropriate lab safety and import restrictions.

Data and code availability

The scRNA-seq datasets generate for this study are available from Gene Expression Omnibus Accession GSE284262. All analysis scripts and processed data are available (https://drive.google.com/drive/folders/1Qnv4TorlnZ5z_Z6yzBMwJAIleGyXP9x9?usp=drive_link).

EXPERIMENTAL MODEL AND SUBJECT DETAILS

Ethics Statement

All Tha RABV *in vitro* infections were performed under BSL3 containment in accordance with the biosafety protocols developed and approved by the Pasteur Institute.

Human brain cell type co-culture

Human neural stem cell culture and differentiation

Human neuronal stem cells (hNSC, EnStem-A™ SCC003, Millipore) were amplified on plates previously cultured with geltrex (A1413201, Invitrogen) in complete neural stem cell (CNSC) medium containing Knock-out D-MEM/F-12 (A1370801, Thermo Fisher), 2 mM Glutamax (35050038, Thermo Fisher), 2% StemPro Neural Supplement (A1050801, ThermoFisher), 20 ng/ml human FGF (PHG0026, Thermo Fisher), and 20 ng/mL human EGF (PHG0311, Thermo Fisher) at 37°C and 5% CO_2. For differentiation, hNSC cells were seeded at a density of $1.5x10^5$ cells/cm^2 on plates previously coated with poly-ornithine (P4957, Sigma-Aldrich) and

1591 laminin (L2020, Sigma-Aldrich). One day after seeding, the medium was changed to
1592 differentiation medium containing neurobasal medium (10888022, Thermo Fisher), 2 mM
1593 Glutamax (35050038, Thermo Fisher), 2% B-27 serum free supplement (17504044, Thermo
1594 Fisher), 200 μM Ascorbid acid (A4403, Sigma-Aldrich) and 1x Penicillin/Streptomycin
1595 (15140148, Thermo Fisher). Human NSC were differentiated for one week before hiMacs were
1596 added to the culture. Half of the medium was changed every third day.
1597
1598 ***Differentiation of hiPSCs to hiMacs***
1599 Human induced macrophage-like cells (hiMacs) were generated from iPSCs according to a
1600 published method described by Takata *et al*[126]. In short, 5 ng/mL BMP-4 (314-BP-050, R&D
1601 Systems), 50 ng/mL VEGF (293-VE-500, R&D Systems), 2 μM CHIR99021 (4423, TOCRIS)
1602 induced mesoderm specification of human iPSC colonies (XCL-1) and hemangioblast-like cell
1603 formation (36). Replacement of CHIR99021 by 20 ng/mL FGF-2 (223-FB-500, R&D Systems),
1604 followed by maintenance in 15 ng/mL VEGF and 5 ng/mL FGF-2 induced differentiation into
1605 the hematopoietic lineage according to a modified protocol from Grigoriadis *et al.* (37). Wnt
1606 signalling was inhibited and hematopoietic stem cells were matured by incubation with 50 ng/ml
1607 SCF (255-SC-01M), 10 ng/mL FGF-2, 20 ng/mL IL-3 (203-IL-050, R&D Systems), 10 ng/mL
1608 IL-6 (206-IL-050, R&D Systems), 10 ng/mL VEGF and 30 ng/mL DKK-1 (5439-DK-500) for 6
1609 days and with 50 ng/mL SCF, 10 ng/mL FGF-2, 20 ng/mL IL-3 and 10 ng/mL IL-6 for 4 days.
1610 To promote terminal differentiation of hiMacs, cells were cultured with 50 ng/mL CSF-1 (216-
1611 MC-01M, R&D Systems) for 14 days (38–40).
1612
1613 ***Differentiation of hiMacs to hiMicros***
1614 After hiMacs generation, hiMacs were co-cultured with 70 – 80 % confluent one week old (day
1615 0 = induction of neural induction) hiNeurons and hiAstrocytes for three consecutive weeks. In
1616 detail, 7 days after the induction of neural differentiation, $1x10^4$ cells/cm^2 hiMacs were added
1617 to the $1.5x10^5$ cells/cm^2 hiNeurons and hiAstrocytes. Half of the culture medium was changed
1618 every third day supplemented with 50 ng/mL recombinant human CSF-1 (216-MC-010, R&D
1619 Systems) and 50 ng/mL human IL-34 (5265-IL-010, R&D Systems). Cells were co-cultured for
1620 three consecutive weeks before infection experiments were started.
1621
1622 **Tha RABVs**
1623 Thailand virus, referred to as 8764THA (Genbank No. EU293111) is a field strain of RABV
1624 isolated from the brain of a Thai patient who died of RABV after being bitten by a rabid dog
1625 (EVAg collection, Ref-SKU: 014V-02106) (29). This virus was further adapted to cell culture
1626 on BSR cells (a BHK-21 clone, kindly provided by Monique Lafon, Institute Pasteur, Paris)
1627 (32), consequently called 8743THA (Genbank No. EU293121) (29) and in this manuscript
1628 referred to as “Tha”. The recombinant Tha2P4M RABV harbors the same genetic background
1629 as Tha apart from bearing two point mutations in the viral P-protein (W265G, M287V) and four
1630 mutations in the viral M-protein (R77K, D100A, A104S, M110L) which were previously
1631 described (15,21,33). To validate viral infection, recombinant viral Tha-eGFP and Th2P4M-
1632 eGFP constructs were used which were generated by cloning sequences of eGFP (recovered
1633 from pEGFP-C1 plasmid, Promega) into the genetic sequence of Tha (34) and Th2P4M,
1634 respectively. Viral strains were sequenced before used for infection experiments. Viral titers
1635 were determined by virus titration on BSR cells via staining of the viral nucleoprotein (5100,
1636 Sigma-Aldrich).
1637

1638 **METHOD DETAILS**

1639 **Visualizing 2P4M mutations on P and M protein structures**

1640 ChimeraX (v1.8)[127] was used to highlight the P protein (W265G, M287V) substitutions on the
1641 structure of the P protein from RABV CVS-11 strain (Protein Data Bank Accession: 1vyi) and
1642 four mutations in the M protein (R77K, D100A, A104S, M110L) on the M protein from Lagos
1643 bat virus (Protein Data Bank Accession: 2W2S). Amino acid alignments (using the CLUSTALW
1644 algorithm implemented in SnapGene (v7.2.1)) confirmed the conserved site positions of each
1645 mutation across lyssavirus species and strains (**Figure S1F**).
1646

1647 **Tha RABV infection conditions**

1648 After four weeks of differentiation *in vitro*, co-cultured human brain cells were subject to Tha
1649 RABV infection through bath-application of Tha RABV (diluted in 500 ul of differentiation
1650 media) versus mock infections (500 ul of differentiation media alone) for two hours at 37°C and
1651 5% CO_2. To visualize infected cells and confirm identities of infected cell types, Tha RABV
1652 expressing GFP (Tha-eGFP, MOI 0.5) was used following post-hoc immunofluorescence
1653 analysis. To generate co-cultures upstream of single-cell RNA sequencing, infections were
1654 performed with Tha (MOI 0.5 or 5.0), Tha2P-4M (MOI 0.5) or "No Infection" (mock infection)
1655 were performed.
1656

1657 **Immunofluorescence-based identification of Tha RABV infected cell types**

1658 Forty-eight hours post-infection, co-cultures were fixed using 4% PFA for 15 minutes at room
1659 temperature. After fixation, cells were then washed with PBS (10010023, Thermo Scientific)
1660 and permeabilized using 0.5% triton X-100 (648463, Millipore) for 10 minutes. Immunolabeling
1661 was performed with primary and secondary antibodies (Key resources table) using the
1662 following staining conditions: Cells were stained with the primary antibody diluted in PBS
1663 (10010023, Thermo Scientific) supplemented with 5% heat-inactivated fetal bovine serum
1664 (S182H-500, Eurobio) overnight at 4°C according to the manufacturer's instructions.
1665 Subsequently, cells were washed using PBS (10010023, Thermo Scientific), followed by
1666 staining with the secondary antibody for 30 minutes at 37°C according to the manufacturer's
1667 instructions. Immunolabeled cultures were washed using PBS (10010023, Thermo Scientific)
1668 and imaged using the Opera Phenix™ High Content Screening System (Perkin Elmer) using
1669 standard conditions.
1670

1671 **Single-cell RNA sequencing data generation and processing**

1672 Forty-eight hours after infection, cells were dissociated using StemPro Accutase (A1110501,
1673 Thermo Scientific) supplemented with 50 U/mL papain (P4762, Sigma Aldrich). In detail, cells
1674 were incubated in 400 μl dissociation solution for 10 minutes at 37°C. After 10 minutes, cells
1675 were resuspended in neurobasal medium (10888022, Thermo Fisher) supplemented with 2%
1676 heat-inactivated fetal bovine serum (S182H-500, Eurobio) and 10 μM ROCK inhibitor Y-27632
1677 (ACS-3030, Stemcell Technologies). Cells were centrifuged at 1000 *rpm* for 5 minutes at 4°C.
1678 Viability was increased by removing dead cells via the Dead Cell Removal Kit (130-090-101,
1679 Miltenyi Biotec). In short, cells were resuspended in 100 μl of dead cell removal beads. After
1680 15 minutes of incubation, 400 μl of binding buffer was added to each sample. Samples were
1681 added to the freshly washed LS columns (130-042-401, Miltenyi Biotec). Columns were
1682 washed with 4.5 mL binding buffer (Miltenyi Biotec) and the flow-through was collected. After
1683 the collection of viable cells, cells were centrifuged at 1000 *rpm* for 5 minutes at 4°C.
1684 Meanwhile, viable cells were counted and diluted to a final concentration of 1000 cells/μl.
1685 10,000 cells were loaded per condition using the Chromium Next GEM Single Cell 3' Reagent

Kit v3.1 (PN-1000128, 10x Genomics). The 10x libraries were sequenced at a depth of 40,000 reads per cell using the Illumina NovaSeq Instrument (Novogene). CellRanger (10x Genomics; v5.0.1) was used to align reads against a composite human (GRCh38) and Tha RABV genome. Digital Gene Expression (DGE) matrices were generated using reads mapped to gene exons.

scRNA-seq workflow for analysis of Tha RABV and human gene expression

Single-cell RNA-seq data was analyzed in two distinct ways to study human and viral gene expression in an independent manner and in a synergistic manner in which viral and human RNAs were associated with the same RNA profiles using experiment-specific cell barcodes.
First, to study human gene expression patterns without the influence of Tha RABV RNAs, Tha RABV genes were removed to create human-specific DGEs. Human-specific DGEs across all experimental conditions were filtered based on quality control metrics (described below) and then processed using a standard workflow in Seurat (v4.4.0)[112] to clustering RNA profiles, revealing cell type identities. Specifically, scRNA libraries were filtered to include those libraries with >2,500 UMIs and % of mitochondrial RNAs meeting custom thresholds based on library size (**Figure S2A**; range: 1-19.9 %). UMI counts in each library were then log-normalized (*NormalizeData(normalization.method = "LogNormalize", scale.factor = 10000)*) and expression values for each gene were centered (*ScaleData()*). Clustering was then performed after variable gene selection (*FindVariableFeatures()* and *RunPCA()*), using n=15 principal components as input for shared nearest-neighbor graph construction (*FindNeighbors(dims=1:15)*). Clustering was then performed with the smart local moving algorithm (*FindClusters(resolution=0.12)*) and a UMAP embedding was generated (*RunUMAP(dims=1:15, min.dist=0.4))* for visualization. Cell type identities for each cluster were assigned by evaluating the expression patterns of well-established cell-type-specific marker genes for neurons, astrocytes, microglia, neural stem cells and mitotic cell (**Figure S2E**). Second, an “infection summary” file was generated to study Tha RABV gene expression at single-cell resolution. The summary infection file includes UMI counts for each Tha RABV gene as well as total Tha RABV and grand total UMIs (human + Tha). Cell type and infection-status identities (see below) were then assigned to the Tha infection file using experiment-specific cell barcodes for downstream analysis. Importantly, to avoid confounds of low-quality libraries, only those RNA profiles passing the quality-control metrics and included in the final Seurat analysis were included for analyses of Tha gene expression. After global clustering analysis, astrocyte and microglia cellular RNA profiles were independently analyzed in Seurat using a similar workflow. In each case, subclustering revealed minor groups of RNA profiles that exhibited gene expression signatures of other cell types or high-levels of nuclear lncRNAs and thus were removed as candidate “doublets” or low-quality cellular RNA profiles.

Identification of infected and uninfected cells using expectation-maximization

The observed Tha RABV viral RNA UMI counts were modelled as a mixture of two compound log-normal-binomial distributions, one for each of the populations of infected and uninfected cells. These compound distributions were also regressed by the total UMIs for each profile (i.e. library size), allowing the model to account for differences infectivity across cell type populations with varying library sizes. Specifically, letting *LS = library size (total Tha + human UMIs)*, *VL = viral load (% of UMIs from Tha)*, and *VC = viral counts (total Tha UMIs)*, for a given cell with index *i* we draw:
*VL_i ~ logNormal (mu_offset + mu_coef * log (LS_i), sigma_offset + sigma_coef * log(LS_i))*
and then:

VC_i ~ Binom (VL_i, LS_i)

where the parameters *mu_offset*, *mu_coef*, *sigma_offset*, and *sigma_coef* are learned separately for the populations of infected and uninfected cells. The conjugate prior distribution for the binomial distribution is the beta distribution, but we found the beta distribution to fit the expression data poorly, which we hypothesize is due to numerical instability arising from the extreme skew towards low viral load in our data. We chose instead to use a log-normal distribution as the prior distribution for VL, with the additional restriction 0 <= VL <= 1. (In practice, the missing/erroneous probability density from VL > 1 is negligible). Parameter learning was accomplished with a standard expectation-maximization algorithm, first randomly assigning each cell to one of two groups, which we will later categorize as infected or uninfected. For the maximization step, we fit a log-normal-binomial compound distribution (via maximum likelihood estimation) for each population of cells, as well as estimating the priors for each cell belonging to either group. To find maximum likelihood estimates for the log-normal-binomial distributions, we computed and maximized likelihood using the R language optimizer "optim" function, with "method = 'Nelder-Mead'" and starting parameters `mu_off = -4, mu_coef = -0.1, sigma_off = 1.5, sigma_coef = 0`. The probability density for the log-normal-binomial distribution was computed by grid approximation (using 200 points evenly spaced between [-15, 0] and exponentiated). For the expectation step, each cell was assigned to the fitted model from the previous step that maximized its posterior probability. Then new compound log-normal-binomial distributions were fit to the reassigned groups of cells, and the cells recategorized, repeating this process until convergence (n=20 iterations).

Gene expression plotting

Gene expression levels were plotted using normalized, gene-centered data using functions from Seurat or custom plotting functions using the "ggplot2" (v3.5.1)[115] R package.

Bulk and scRNA-seq analysis of Tha read alignment and gene expression

We re-analyzed bulk mRNA expression data from Tha RABV infection of BSR cells (Gene Expression Omnibus accession GSE178583) in addition to Tha RABV scRNA-seq data from human brain cell type co-cultures to compare Tha RABV gene expression levels and read alignment locations across sequencing modalities (**Figure S3A,B**). Bulk mRNA sequencing data was generated with the TruSeq Stranded mRNA library kit (Illumina). In the previous publication[35], bulk mRNA data were aligned and analyzed with respect to only the human genome (reference GRCh38). Thus STAR (v2.7.9a)[110] was used to realign the bulk mRNA fastq files to both the human and Tha genomes followed by RSEM (v1.3.1)[111] to quantify Tha RABV gene expression levels using transcripts per million reads (TPM) values. Sequencing read coverage against the Tha genome was assessed for the bulk mRNA data and ten randomly selected cell barcodes from the scRNA-seq associated with the neurons, cluster 1 and pro-viral cluster 2 astrocytes. To do this, BAM files associated with these specific read sets were converted to bigwig files then read alignment coordinates were exported to csv files for analysis in R.

Tha RABV gene expression analysis from scRNA-seq data

Viral mRNA load scores were calculated for each cell's RNA profile as the percentage of total UMIs (human + Tha) attributed to the five genes in Tha RABV genome (*N, P, M, G* and *L*). Relative expression of each Tha RABV gene was calculated based on the UMIs associated with each gene versus the total Tha RABV UMIs for each cellular RNA profile. To avoid biases driven by insensitive mRNA detection, analysis was limited to cellular RNA profiles with > 0

1782 UMIs for *G* and *L* (the Tha genes with the lowest expression levels; **Figure S3B**). A one-way
1783 ANOVA was used to test for differences in Tha gene expression levels, while a two-way
1784 ANOVA was used to evaluate if cell type and experimental condition affected relative
1785 expression of each Tha gene. Pairwise testing of differences Tha gene expression by cell type
1786 and experimental condition was performed using the Kolmogorov–Smirnov test. P values are
1787 reported as uncorrected.
1788
1789 **Differential expression testing**
1790 Human gene differential expression testing across experimental conditions or cell types was
1791 implemented in the "Libra" (v1.0.0) R package using the DESeq2 likelihood ratio test method
1792 (*Libra::run_de(de_method="DESeq2", de_type="LRT")*). All reported and analyzed p values
1793 are corrected for multiple hypothesis testing using the Benjamini-Hochberg method.
1794
1795 **Gene Set Enrichment REACTOME analysis**
1796 Gene Set Enrichment Analysis (GSEA) and REACTOME Analysis were performed using the
1797 "clusterProfiler" (v4.8.3)[116] and the ReactomePA(v1.44)[118] R packages, respectively. GSEA
1798 assessed the "Biological Pathways" ontology using a gene-specific score based on multiplying
1799 the -log10(p value) * log2FC for each gene across Tha2P4M(0.5) versus Tha(0.5) astrocytes
1800 (*clusterProfiler::gseGO(ont = 'BP',OrgDb = 'org.Hs.eg.db', eps=1e-300)*). The ten Biological
1801 Pathways with strongest enrichment scores visualized using the enrichplot (v1.20.3) R
1802 package (*enrichplot::gseaplot2(= 1:10, ES_geom = "line"*). REACTOME analysis was
1803 performed on differentially expressed gene sets ($p < 0.01$) enriched in either Cluster 1 (n=2,137
1804 genes) or Cluster 2 (n=5,887 genes) Astrocytes ($p < 0.01$)
1805 (ReactomePA::enrichPathway(pvalueCutoff = 0.01). To discern structure within complex
1806 REACTOME results, hierarchical clustering was performed for the most enriched REACTOME
1807 categories Cluster 1 ($p < 0.000001$; n = 32 categories) and Cluster 2 ($p < 0.01$; n = 84
1808 categories) based on similarities of gene driving each categorical enrichment. These results
1809 were visualized using the treeplot() function from the enrichplot (v1.20.3) R package.
1810 REACTOME p values are computed from the hypergeometric distribution using a one-sided
1811 Fisher's exact test and corrected for multiple comparisons using the Benjamini–
1812 Hochberg method.
1813
1814 **Analysis of cell-cell interaction using CellPhoneDB**
1815 "CellPhoneDB"[105] (v5.0; implemented in Python v3.8.19) was used to infer "relevant"
1816 differences in cell-cell interactions between Cluster 1 and pro-viral Cluster 2 astrocytes across
1817 the scRNA-seq dataset. Specifically, "relevant" interactions were identified from the list of
1818 differentially expressed genes comparing Cluster 1 and pro-viral Cluster 2 ($p < 0.01$; LFC > 1;
1819 n= 2,186 enriched in Cluster 1; n= 877 enriched in Cluster 2), a subset of which encode ligands
1820 (n=427) or receptors (n=341). "Relevant" interactions were those that were selectively enriched
1821 in either astrocyte cluster following the CellPhoneDB gene shuffling approach across all cell-
1822 type clusters (neurons, microglia, hNSC and mitotic) from full scRNA-seq dataset ($p < 0.05$).
1823 The "relevant_interactions" CellPhoneDB output file was used for downstream analysis,
1824 visualization and plotting in R including, the R package "circlize" (v0.4.16)[123].
1825
1826 **Pseudotime trajectory analysis astrocytes using Monocle3**
1827 "Monocle3" was used to perform a pseudotime-based trajectory analysis of astrocyte
1828 transcriptional diversity following a standard workflow based on six principal components that
1829 describe gene expression variation across the human genome. Pseudotime relationships were

visualized both through both a UMAP embedding and in a linear fashion after binning scRNA profiles into 40 pseudotime-ordered bins (n=99 or 100 scRNA profiles per bin). Experimental identities associated with the cells in each bin were analyzed as proportions (Cluster 1 and Cluster 2 identities from the Seurat analysis or experimental origin). Viral mRNA load scores were also plotted by bin. To visualize expression signatures of genes induced in pro-viral Cluster 2 ($p < 0.01$; LFC > 1) across pseudotime bins, bin-specific average expression values were calculated and normalized to maximum expression value to facilitate cross-gene comparisons. Genes were then catergorized by pseudotime expression profile. To do this, each gene's expression profile was visually inspected. Genes with minimal expression fluctuation before bin 36 yet a clear increase in expression at bin 37 were categorized as "Early". Genes with minimal fluctuation before bin 36 but were categorized into (mutally exclusive) "Progressive", "Sustained", "Transient" or "Late" categories based on expression patterns across bins 38-40.

Random forest regression analysis of human gene RNA levels and viral mRNA load

Random Forest regression analysis was performed using the randomForest(v4.7-1.2) R package independently for neurons, Cluster 1 astrocytes and pro-viral Cluster 2 astrocytes. Viral mRNA load scores were used as the dependent variable and normalized gene expression values for those n=11,943 genes that passed expression threshold criteria for differential expression testing using Libra. Regression results were generated from n=200 trees and importance scores were retained using default parameters (*randomForest(ntree=200, keep.forest=FALSE, importance=TRUE, do.trace = 5*).

Identification of pro-viral Cluster 2-like Astrocytes in the NPH snRNA-seq dataset

To test for evidence of pro-viral Cluster 2-like astrocytes in the human brain without confounds of post-mortem interval, we took advantage of a published snRNA-seq dataset profiled from flash-frozen cortical tissue acquired during surgical treatment of Normal Pressure Hydrocephalus[79]. We used RNA count data and associated patient-specific metadata from the subset of snRNA-seq profiles belonging to astrocytes (n= 82,634 profiles; https://zenodo.org/records/8319719). The RNA count data were cell-normalized and gene-centered using the standard Seurat workflow (equivalent to the processing performed on the Tha scRNA-seq dataset). To identify potential Cluster 2-like astrocytes from these NPH data, we generated an aggregate expression score based on the n=196 genes observed in the NPH data and enriched in Cluster 2 ($p <0.01$ and 2 > log2 fold-change). To critically evaluate the biological significance of these aggregate expression scores, we generated 1,000 expression-matched sets of 196 genes. Expression-matching was performed by rank-ordering the NPH genes by expression level; dividing these expression-ranked genes into ten bins from low to high expression; and randomly sampling (without replacement) each bin by the number of instances of each of the 196 Cluster 2 enriched genes. To facilitate comparison of the real and permuted aggregate gene score distributions, each of 82,634 scores were z-scored by gene list and z-score distributions were then analyzed (**Figure 4H**). A z-score threshold of 4.5 standard deviations was used to identify n=38 Cluster 2-like NPH astrocytes contributed by n=21 of 52 total patients (n=1 to 4 Cluster 2-like NPH astrocytes in each of those 21 patients; z-score range: 4.5 – 12.5). The cut-off of 4.5 standard deviations corresponds to a p-value of < 4.7E-7 based on the permuted data. To validate these 38 astrocyte RNA profiles resembled those of Cluster 2, we tested whether gene counts associated with the 196 "discovery" gene set and an independent "validation" gene set of RNAs enriched in Cluster 2 ($p <0.01$ and 1-2 log2 fold-change; n=521 genes) were enriched in the 38 Cluster 2-like astrocytes versus all

other NPH astrocyte RNA profiles (n=82,596). The discovery and validation gene counts were 2.8 and 1.2 enriched respectively in the 38 Cluster 2-like NPH astrocytes and highly significant (chi-square test of expected versus observed UMIs; $p < 1E-16$).

Comparing "reactive" astrocyte gene signatures from other datasets to pro-viral Cluster 2 astrocytes

To assess the similarity of previously reported rodent and human reactive astrocyte gene expression signatures to those observed in pro-viral Cluster 2 astrocytes, we re-analyzed data from *ex vivo* mouse astrocytes stimulated with lipopolysaccharides (Hasel et al; scRNA-seq data)[81] or cultured rat and human astrocytes stimulated with TNF, IL1α, C1Q, and IFNβ, a cocktail that induces an interferon-responsive reactive state (Prakash et al; RNA and proteomic profiling)[80]. Specifically, for Hasel et al, gene enrichment data from the ten scRNA-seq-defined astrocyte clusters were downloaded (Supplementary Table 5). Analysis focused on those genes enriched in cluster 8 (n=70 genes), an astrocyte sub-population described by Hasel et al as "interferon reactive"[81]. For Prakash et al, RNA and protein enrichments associated with rat and human interferon-responsive state were downloaded (Supplementary Tables 3 and 5). Analysis focused on the n=67 rat genes with concordant, statistically-significant enrichments in both RNA and protein; for human astrocytes, analysis focused on the n=8 genes enriched via proteomic analysis (RNA expression data was not acquired). The genes from these three lists were visualized on volcano plots describing Cluster 1 versus pro-viral Cluster 2 differentially expressed genes. In all three cases, RNAs from the published gene set showed no obvious enrichments for those genes differentially expressed in Cluster 1 or pro-viral Cluster 2 and thus no statistical test was performed.

Analysis of single-cell RNA sequencing data

Statistical testing and plot generation was performed in R (v4.3.0; R packages are provided in the Key Resources table). All p-values are reported as adjusted for multiple-hypothesis testing unless otherwise stated. Test-specific information is included the relevant STAR Methods sections.

References

1. Hampson, K. *et al.* Estimating the Global Burden of Endemic Canine Rabies. *PLoS Neglected Trop. Dis.* **9**, e0003709 (2015).

2. Schnell, M. J., McGettigan, J. P., Wirblich, C. & Papaneri, A. The cell biology of rabies virus: using stealth to reach the brain. *Nat Rev Micro* 1–11 (2009) doi:10.1038/nrmicro2260.

3. Jackson, A. C., Randle, E., Lawrance, G. & Rossiter, J. P. Neuronal apoptosis does not play an important role in human rabies encephalitis. *J. NeuroVirology* **14**, 368–375 (2008).

4. Suja, M. S., Mahadevan, A., Madhusudana, S. N. & Shankar, S. K. Role of Apoptosis in Rabies Viral Encephalitis: A Comparative Study in Mice, Canine, and Human Brain with a Review of Literature. *Pathol. Res. Int.* **2011**, 374286 (2011).

5. Griffin, D. E. Recovery from viral encephalomyelitis: immune-mediated noncytolytic virus clearance from neurons. *Immunol. Res.* **47**, 123–133 (2010).

1921 6. Yordy, B., Iijima, N., Huttner, A., Leib, D. & Iwasaki, A. A Neuron-Specific Role for
1922 Autophagy in Antiviral Defense against Herpes Simplex Virus. *Cell Host Microbe* **12**, 334–
1923 345 (2012).

1924 7. Potratz, M. *et al.* Astrocyte Infection during Rabies Encephalitis Depends on the Virus
1925 Strain and Infection Route as Demonstrated by Novel Quantitative 3D Analysis of Cell
1926 Tropism. *Cells* **9**, 412–20 (2020).

1927 8. Potratz, M. *et al.* Neuroglia infection by rabies virus after anterograde virus spread in
1928 peripheral neurons. *Acta Neuropathol. Commun.* **8**, 199 (2020).

1929 9. Feige, L. *et al.* Susceptibilities of CNS Cells towards Rabies Virus Infection Is Linked to
1930 Cellular Innate Immune Responses. *Viruses* **15**, 88 (2022).

1931 10. Pfefferkorn, C. *et al.* Abortively Infected Astrocytes Appear To Represent the Main
1932 Source of Interferon Beta in the Virus-Infected Brain. *J Virol* **90**, 2031–2038 (2016).

1933 11. Sofroniew, M. V. Astrocyte Reactivity: Subtypes, States, and Functions in CNS Innate
1934 Immunity. *Trends Immunol.* **41**, 758–770 (2020).

1935 12. Sugamata, M. *et al.* Paralysis of street rabies virus-infected mice is dependent on T
1936 lymphocytes. *J. Virol.* **66**, 1252–1260 (1992).

1937 13. Zhao, P. *et al.* Global gene expression changes in BV2 microglial cell line during rabies
1938 virus infection. *Infect., Genet. Evol.* **20**, 257–269 (2013).

1939 14. Bertoune, M. A. R. *et al.* The phenotype of the RABV glycoprotein determines cellular
1940 and global virus load in the brain and is decisive for the pace of the disease. *Virology* **511**,
1941 82–94 (2017).

1942 15. Khalifa, Y. B. *et al.* The matrix protein of rabies virus binds to RelAp43 to modulate NF-
1943 κB-dependent gene expression related to innate immunity. *Sci. Rep.* **6**, 39420 (2016).

1944 16. Besson, B. *et al.* Regulation of NF-κB by the p105-ABIN2-TPL2 complex and RelAp43
1945 during rabies virus infection. *PLoS Pathog.* **13**, e1006697 (2017).

1946 17. Vidy, A., Chelbi-Alix, M. & Blondel, D. Rabies Virus P Protein Interacts with STAT1 and
1947 Inhibits Interferon Signal Transduction Pathways. *J Virol* **79**, 14411–14420 (2005).

1948 18. Brzózka, K., Finke, S. & Conzelmann, K.-K. Inhibition of Interferon Signaling by Rabies
1949 Virus Phosphoprotein P: Activation-Dependent Binding of STAT1 and STAT2. *J. Virol.* **80**,
1950 2675–2683 (2006).

1951 19. Lieu, K. G. *et al.* The Rabies Virus Interferon Antagonist P Protein Interacts with
1952 Activated STAT3 and Inhibits Gp130 Receptor Signaling. *J. Virol.* **87**, 8261–8265 (2013).

1953 20. Sonthonnax, F. *et al.* Lyssavirus matrix protein cooperates with phosphoprotein to
1954 modulate the Jak-Stat pathway. *Sci. Rep.* 1–13 (2019) doi:10.1038/s41598-019-48507-4.

1955 21. Wang, Z. W. *et al.* Attenuated Rabies Virus Activates, while Pathogenic Rabies Virus
1956 Evades, the Host Innate Immune Responses in the Central Nervous System. *J Virol* **79**,
1957 12554–12565 (2005).

1958 22. Ménager, P. *et al.* Toll-Like Receptor 3 (TLR3) Plays a Major Role in the Formation of
1959 Rabies Virus Negri Bodies. *PLoS Pathog* **5**, e1000315-15 (2009).

1960 23. Lahaye, X., Vidy, A., Fouquet, B. & Blondel, D. Hsp70 Protein Positively Regulates
1961 Rabies Virus Infection. *J Virol* **86**, 4743–4751 (2012).

1962 24. Daugherty, M. D. & Malik, H. S. Rules of Engagement: Molecular Insights from Host-
1963 Virus Arms Races. *Annu. Rev. Genet.* **46**, 677–700 (2012).

1964 25. Abraham, G. & Banerjee, A. K. Sequential transcription of the genes of vesicular
1965 stomatitis virus. *Proc. Natl. Acad. Sci.* **73**, 1504–1508 (1976).

1966 26. Ball, L. A. & White, C. N. Order of transcription of genes of vesicular stomatitis virus.
1967 *Proc. Natl. Acad. Sci.* **73**, 442–446 (1976).

1968 27. Ball, L. A. Transcriptional mapping of vesicular stomatitis virus in vivo. *J. Virol.* **21**, 411–
1969 414 (1977).

1970 28. Vidy, A., Bougrini, J. E., Chelbi-Alix, M. K. & Blondel, D. The Nucleocytoplasmic Rabies
1971 Virus P Protein Counteracts Interferon Signaling by Inhibiting both Nuclear Accumulation and
1972 DNA Binding of STAT1. *J. Virol.* **81**, 4255–4263 (2007).

1973 29. Hossain, Md. A. *et al.* Structural Elucidation of Viral Antagonism of Innate Immunity at the
1974 STAT1 Interface. *Cell Rep.* **29**, 1934-1945.e8 (2019).

1975 30. Harrison, A. R. *et al.* Lyssavirus P-protein selectively targets STAT3-STAT1 heterodimers
1976 to modulate cytokine signalling. *PLoS Pathog.* **16**, e1008767 (2020).

1977 31. Scrima, N. *et al.* Rabies virus P protein binds to TBK1 and interferes with the formation of
1978 innate immunity-related liquid condensates. *Cell Rep.* **42**, 111949 (2023).

1979 32. Wang, Z. *et al.* Substitution of S179P in the Lyssavirus Phosphoprotein Impairs Its
1980 Interferon Antagonistic Function. *J. Virol.* **96**, e01125-22 (2022).

1981 33. Masatani, T. *et al.* Contribution of the interaction between the rabies virus P protein and I-
1982 kappa B kinase ϵ to the inhibition of type I IFN induction signalling. *J. Gen. Virol.* **97**, 316–326
1983 (2016).

1984 34. Wiltzer, L. *et al.* Interaction of Rabies Virus P-Protein With STAT Proteins is Critical to
1985 Lethal Rabies Disease. *J. Infect. Dis.* **209**, 1744–1753 (2014).

1986 35. Kim, S. *et al.* Early Transcriptional Changes in Rabies Virus-Infected Neurons and Their
1987 Impact on Neuronal Functions. *Front Microbiol* **12**, 730892 (2021).

1988 36. Zhang, D. *et al.* Genome-Wide Transcriptional Profiling Reveals Two Distinct Outcomes
1989 in Central Nervous System Infections of Rabies Virus. *Front. Microbiol.* **7**, 118–16 (2016).

1990 37. Huang, K. W. & Sabatini, B. L. Single-Cell Analysis of Neuroinflammatory Responses
1991 Following Intracranial Injection of G-Deleted Rabies Viruses. *Front Cell Neurosci* **14**, 65
1992 (2020).

1993 38. Raux, H., Flamand, A., virology, D. B. J. of & 2000. Interaction of the rabies virus P
1994 protein with the LC8 dynein light chain. *Am Soc Microbiol*.

1995 39. Tan, G. S., Preuss, M. A. R., Williams, J. C. & Schnell, M. J. The dynein light chain 8
1996 binding motif of rabies virus phosphoprotein promotes efficient viral transcription. *Proc. Natl.*
1997 *Acad. Sci.* **104**, 7229–7234 (2007).

1998 40. Poisson, N. *et al.* Molecular basis for the interaction between rabies virus phosphoprotein
1999 P and the dynein light chain LC8: dissociation of dynein-binding properties and
2000 transcriptional functionality of P. *J. Gen. Virol.* **82**, 2691–2696 (2001).

2001 41. Jespersen, N. E. *et al.* The LC8-RavP ensemble Structure Evinces A Role for LC8 in
2002 Regulating Lyssavirus Polymerase Functionality. *J. Mol. Biol.* **431**, 4959–4977 (2019).

2003 42. Bauer, A., Nolden, T., Nemitz, S., Perlson, E. & Finke, S. A Dynein Light Chain 1 Binding
2004 Motif in Rabies Virus Polymerase L Protein Plays a Role in Microtubule Reorganization and
2005 Viral Primary Transcription. *J Virol* **89**, 9591–9600 (2015).

2006 43. Ouyang, J. *et al.* NRAV, a Long Noncoding RNA, Modulates Antiviral Responses through
2007 Suppression of Interferon-Stimulated Gene Transcription. *Cell Host Microbe* **16**, 616–626
2008 (2014).

2009 44. Shetty, A. *et al.* A systematic comparison of FOSL1, FOSL2 and BATF-mediated
2010 transcriptional regulation during early human Th17 differentiation. *Nucleic Acids Res.* **50**,
2011 4938–4958 (2022).

2012 45. Comandante-Lou, N., Baumann, D. G. & Fallahi-Sichani, M. AP-1 transcription factor
2013 network explains diverse patterns of cellular plasticity in melanoma cells. *Cell Rep.* **40**,
2014 111147 (2022).

2015 46. Katagiri, T., Kameda, H., Nakano, H. & Yamazaki, S. Regulation of T cell differentiation
2016 by the AP-1 transcription factor JunB. *Immunol. Med.* **44**, 197–203 (2021).

2017 47. Renoux, F. *et al.* The AP1 Transcription Factor Fosl2 Promotes Systemic Autoimmunity
2018 and Inflammation by Repressing Treg Development. *Cell Rep.* **31**, 107826 (2020).

2019 48. Ku, H.-C. & Cheng, C.-F. Master Regulator Activating Transcription Factor 3 (ATF3) in
2020 Metabolic Homeostasis and Cancer. *Front. Endocrinol.* **11**, 556 (2020).

2021 49. James, C. G., Woods, A., Underhill, T. M. & Beier, F. The transcription factor ATF3 is
2022 upregulated during chondrocyte differentiation and represses cyclin D1 and A gene
2023 transcription. *BMC Mol. Biol.* **7**, 30 (2006).

2024 50. Kim, H.-J. *et al.* CREB5 promotes the proliferation and self-renewal ability of glioma stem
2025 cells. *Cell Death Discov.* **10**, 103 (2024).

2026 51. Gingras, S., Pelletier, S., Boyd, K. & Ihle, J. N. Characterization of a Family of Novel
2027 Cysteine- Serine-Rich Nuclear Proteins (CSRNP). *PLoS ONE* **2**, e808 (2007).

2028 52. Feijóo, C. G., Sarrazin, A. F., Allende, M. L. & Glavic, A. Cystein-serine-rich nuclear
2029 protein 1, Axud1/Csrnp1, is essential for cephalic neural progenitor proliferation and survival
2030 in zebrafish. *Dev. Dyn.* **238**, 2034–2043 (2009).

2031 53. Wang, S.-S. *et al.* Early growth response 2 (Egr2) plays opposing roles in committing
2032 C3H10T1/2 stem cells to adipocytes and smooth muscle-like cells. *Int. J. Biochem. Cell Biol.*
2033 **45**, 1825–1832 (2013).

2034 54. Iwata, A. *et al.* Egr2 drives the differentiation of Ly6Chi monocytes into fibrosis-promoting
2035 macrophages in metabolic dysfunction-associated steatohepatitis in mice. *Commun. Biol.* **7**,
2036 681 (2024).

2037 55. Lulli, V. *et al.* Overexpression of Ets-1 in human hematopoietic progenitor cells blocks
2038 erythroid and promotes megakaryocytic differentiation. *Cell Death Differ.* **13**, 1064–1074
2039 (2006).

2040 56. Taveirne, S. *et al.* The transcription factor ETS1 is an important regulator of human NK
2041 cell development and terminal differentiation. *Blood* **136**, 288–298 (2020).

2042 57. Kim, C. J. *et al.* The Transcription Factor Ets1 Suppresses T Follicular Helper Type 2 Cell
2043 Differentiation to Halt the Onset of Systemic Lupus Erythematosus. *Immunity* **49**, 1034-
2044 1048.e8 (2018).

2045 58. Ruan, H. *et al.* Single-cell reconstruction of differentiation trajectory reveals a critical role
2046 of ETS1 in human cardiac lineage commitment. *BMC Biol.* **17**, 89 (2019).

2047 59. Zhang, L. *et al.* Forkhead Box S1 mediates epithelial-mesenchymal transition through the
2048 Wnt/β-catenin signaling pathway to regulate colorectal cancer progression. *J. Transl. Med.*
2049 **20**, 327 (2022).

2050 60. Qiu, J. *et al.* FOXS1 Promotes Tumor Progression by Upregulating CXCL8 in Colorectal
2051 Cancer. *Front. Oncol.* **12**, 894043 (2022).

2052 61. Li, S. *et al.* Hey2 functions in parallel with Hes1 and Hes5 for mammalian auditory
2053 sensory organ development. *BMC Dev. Biol.* **8**, 20 (2008).

2054 62. Gibb, N. *et al.* Hey2 regulates the size of the cardiac progenitor pool during vertebrate
2055 heart development. *Development* **145**, dev167510 (2018).

2056 63. Ozturk, H. *et al.* ISL2 is a putative tumor suppressor whose epigenetic silencing
2057 reprograms the metabolism of pancreatic cancer. *Dev. Cell* **57**, 1331-1346.e9 (2022).

2058 64. Lee, Y. *et al.* Transcriptional control of motor pool formation and motor circuit connectivity
2059 by the LIM-HD protein Isl2. *eLife* **12**, e84596 (2023).

2060 65. Dong, J.-T. & Chen, C. Essential role of KLF5 transcription factor in cell proliferation and
2061 differentiation and its implications for human diseases. *Cell. Mol. Life Sci.* **66**, 2691–2706
2062 (2009).

2063 66. Aksoy, I. *et al.* Klf4 and Klf5 differentially inhibit mesoderm and endoderm differentiation
2064 in embryonic stem cells. *Nat. Commun.* **5**, 3719 (2014).

2065 67. Kinisu, M. *et al.* Klf5 establishes bi-potential cell fate by dual regulation of ICM and TE
2066 specification genes. *Cell Rep.* **37**, 109982 (2021).

2067 68. Bell, S. M. *et al.* Kruppel-like factor 5 is required for formation and differentiation of the
2068 bladder urothelium. *Dev. Biol.* **358**, 79–90 (2011).

2069 69. Oishi, Y. *et al.* Krüppel-like transcription factor KLF5 is a key regulator of adipocyte
2070 differentiation. *Cell Metab.* **1**, 27–39 (2005).

2071 70. Potthoff, M. J. & Olson, E. N. MEF2: a central regulator of diverse developmental
2072 programs. *Development* **134**, 4131–4140 (2007).

2073 71. Li, H. *et al.* Transcription factor MEF2C influences neural stem/progenitor cell
2074 differentiation and maturation in vivo. *Proc. Natl. Acad. Sci.* **105**, 9397–9402 (2008).

2075 72. Rengarajan, J., Tang, B. & Glimcher, L. H. NFATc2 and NFATc3 regulate TH2
2076 differentiation and modulate TCR-responsiveness of naïve TH cells. *Nat. Immunol.* **3**, 48–54
2077 (2002).

2078 73. Perotti, V. *et al.* NFATc2 is an intrinsic regulator of melanoma dedifferentiation.
2079 *Oncogene* **35**, 2862–2872 (2016).

2080 74. Kao, R. M. *et al.* Pbx4 is Required for the Temporal Onset of Zebrafish Myocardial
2081 Differentiation. *J. Dev. Biol.* **3**, 93–111 (2015).

2082 75. Ning, Y. *et al.* Transcription factor PBX4 regulates limb development and haematopoiesis
2083 in mice. *Cell Prolif.* **57**, e13580 (2024).

2084 76. Joshi, S. *et al.* TEAD transcription factors are required for normal primary myoblast
2085 differentiation in vitro and muscle regeneration in vivo. *PLoS Genet.* **13**, e1006600 (2017).

2086 77. Jeffery, D. *et al.* CENP-A overexpression promotes distinct fates in human cells,
2087 depending on p53 status. *Commun. Biol.* **4**, 417 (2021).

2088 78. Havasi, A. *et al.* Histone Acetyl Transferase (HAT) HBO1 and JADE1 in Epithelial Cell
2089 Regeneration. *Am. J. Pathol.* **182**, 152–162 (2013).

2090 79. Gazestani, V. *et al.* Early Alzheimer's disease pathology in human cortex involves
2091 transient cell states. *Cell* **186**, 4438-4453.e23 (2023).

2092 80. Prakash, P. *et al.* Proteomic profiling of interferon-responsive reactive astrocytes in
2093 rodent and human. *Glia* **72**, 625–642 (2024).

2094 81. Hasel, P., Rose, I. V. L., Sadick, J. S., Kim, R. D. & Liddelow, S. A. Neuroinflammatory
2095 astrocyte subtypes in the mouse brain. *Nat Neuro* 1–36 (2021) doi:10.1038/s41593-021-
2096 00905-6.

2097 82. Breuer, K. *et al.* InnateDB: systems biology of innate immunity and beyond--recent
2098 updates and continuing curation. *Nucleic Acids Res* **41**, D1228-33 (2013).

2099 83. Linder, A. *et al.* Defective Interfering Genomes and the Full-Length Viral Genome Trigger
2100 RIG-I After Infection With Vesicular Stomatitis Virus in a Replication Dependent Manner.
2101 *Front. Immunol.* **12**, 595390 (2021).

2102 84. Aouadi, W. *et al.* Comparative analysis of rabies pathogenic and vaccine strains
2103 detection by RIG-I-like receptors. *Microbes Infect.* **26**, 105321 (2024).

2104 85. Cavalieri, R. L., Havell, E. A., Vilcek, J. & Pestka, S. Induction and decay of human
2105 fibroblast interferon mRNA. *Proc. Natl. Acad. Sci.* **74**, 4415–4419 (1977).

2106 86. Barbar, E. Dynein Light Chain LC8 Is a Dimerization Hub Essential in Diverse Protein
2107 Networks †. *Biochemistry* **47**, 503–508 (2008).

87. Jespersen, N. & Barbar, E. Emerging Features of Linear Motif-Binding Hub Proteins. *Trends Biochem. Sci.* **45**, 375–384 (2020).

88. Merino-Gracia, J., García-Mayoral, M. F. & Rodríguez-Crespo, I. The association of viral proteins with host cell dynein components during virus infection. *FEBS Journal* **278**, 2997–3011 (2011).

89. Lahaye, X., Vidy, A., Fouquet, B. & Blondel, D. Hsp70 Protein Positively Regulates Rabies Virus Infection. *J. Virol.* **86**, 4743–4751 (2012).

90. Jurado, S. *et al.* ATM Substrate Chk2-interacting Zn2+ Finger (ASCIZ) Is a Bi-functional Transcriptional Activator and Feedback Sensor in the Regulation of Dynein Light Chain (DYNLL1) Expression*. *J Biol Chem* **287**, 3156–3164 (2012).

91. Rehwinkel, J. & Gack, M. U. RIG-I-like receptors: their regulation and roles in RNA sensing. *Nat. Rev. Immunol.* **20**, 537–551 (2020).

92. Chelbi-Alix, M. K., Vidy, A., Bougrini, J. E. & Blondel, D. Rabies Viral Mechanisms to Escape the IFN System: The Viral Protein P Interferes with IRF-3, Stat1, and PML Nuclear Bodies. *Journal of Interferon & Cytokine Research* **26**, 271–280 (2006).

93. Patani, R., Hardingham, G. E. & Liddelow, S. A. Functional roles of reactive astrocytes in neuroinflammation and neurodegeneration. *Nat. Rev. Neurol.* **19**, 395–409 (2023).

94. Escartin, C. *et al.* Reactive astrocyte nomenclature, definitions, and future directions. *Nat. Neurosci.* **24**, 312–325 (2021).

95. Valdebenito, S., Castellano, P., Ajasin, D. & Eugenin, E. A. Astrocytes are HIV reservoirs in the brain: A cell type with poor HIV infectivity and replication but efficient cell-to-cell viral transfer. *J. Neurochem.* **158**, 429–443 (2021).

96. Veilleux, C. & Eugenin, E. A. Mechanisms of Zika astrocyte infection and neuronal toxicity. *NeuroImmune Pharmacol. Ther.* **2**, 5–18 (2023).

97. Jorgačevski, J. & Potokar, M. Immune Functions of Astrocytes in Viral Neuroinfections. *Int. J. Mol. Sci.* **24**, 3514 (2023).

98. Jorgačevski, J. *et al.* ZIKV Strains Differentially Affect Survival of Human Fetal Astrocytes versus Neurons and Traffic of ZIKV-Laden Endocytotic Compartments. *Sci. Rep.* **9**, 8069 (2019).

99. Boer, E. C. W. de, Gils, J. M. van & Gils, M. J. van. Ephrin-Eph signaling usage by a variety of viruses. *Pharmacol. Res.* **159**, 105038 (2020).

100. Tian, B. *et al.* Lab-Attenuated Rabies Virus Causes Abortive Infection and Induces Cytokine Expression in Astrocytes by Activating Mitochondrial Antiviral-Signaling Protein Signaling Pathway. *Front. Immunol.* **8**, 2011 (2018).

101. Krause, T. B. & Cepko, C. L. Abortive and productive infection of CNS cell types following in vivo delivery of VSV. *Proc. Natl. Acad. Sci.* **121**, e2406421121 (2024).

102. Ray, N. B., Power, C., Lynch, W. P., Ewalt, L. C. & Lodmell, D. L. Rabies viruses infect primary cultures of murine, feline, and human microglia and astrocytes. *Arch. Virol.* **142**, 1011–1019 (1997).

2147 103. Liu, S. Q., Xie, Y., Gao, X., Wang, Q. & Zhu, W. Y. Inflammatory response and MAPK
2148 and NF-κB pathway activation induced by natural street rabies virus infection in the brain
2149 tissues of dogs and humans. *Virol. J.* **17**, 157 (2020).

2150 104. Zhang, X. *et al.* Derivation of Human Embryonic Stem Cells from Developing and
2151 Arrested Embryos. *Stem Cells* **24**, 2669–2676 (2006).

2152 105. Troulé, K. *et al.* CellPhoneDB v5: inferring cell-cell communication from single-cell
2153 multiomics data. *arXiv* (2023) doi:10.48550/arxiv.2311.04567.

2154 106. Mavrakis, M., McCarthy, A. A., Roche, S., Blondel, D. & Ruigrok, R. W. H. Structure and
2155 Function of the C-terminal Domain of the Polymerase Cofactor of Rabies Virus. *J. Mol. Biol.*
2156 **343**, 819–831 (2004).

2157 107. Graham, S. C. *et al.* Rhabdovirus Matrix Protein Structures Reveal a Novel Mode of
2158 Self-Association. *PLoS Pathog* **4**, e1000251-12 (2008).

2159 108. Delmas, O. *et al.* Genomic Diversity and Evolution of the Lyssaviruses. *PLoS ONE* **3**,
2160 e2057 (2008).

2161 109. Besson, B. *et al.* Kinome-Wide RNA Interference Screening Identifies Mitogen-Activated
2162 Protein Kinases and Phosphatidylinositol Metabolism as Key Factors for Rabies Virus
2163 Infection. *mSphere* **4**, 10.1128/msphere.00047-19 (2019).

2164 110. Dobin, A. *et al.* STAR: ultrafast universal RNA-seq aligner. *Bioinformatics* **29**, 15–21
2165 (2012).

2166 111. Li, B. & Dewey, C. N. RSEM: accurate transcript quantification from RNA-Seq data with
2167 or without a reference genome. *BMC Bioinform.* **12**, 323 (2011).

2168 112. Hao, Y. *et al.* Integrated analysis of multimodal single-cell data. *Cell* **184**, 3573-
2169 3587.e29 (2021).

2170 113. Wickham, H. *et al.* Welcome to the Tidyverse. *J. Open Source Softw.* **4**, 1686 (2019).

2171 114. Wickham, H., Francois, R., Henry, L., Kirill & Vaughan, D. dplyr: A Grammar of Data
2172 Manipulation. (2023).

2173 115. Wickham, H. *Ggplot2: Elegant Graphics for Data Analysis*. (Springer-Verlag New York,
2174 2016).

2175 116. Xu, S. *et al.* Using clusterProfiler to characterize multiomics data. *Nat. Protoc.* 1–29
2176 (2024) doi:10.1038/s41596-024-01020-z.

2177 117. Yu, G. enrichplot: Visualization of Functional Enrichment Result. *R package version*
2178 *1.24.4* (2024).

2179 118. Yu, G. & He, Q.-Y. ReactomePA: an R/Bioconductor package for reactome pathway
2180 analysis and visualization. *Mol. Biosyst.* **12**, 477–479 (2015).

2181 119. Slowikowski, K. ggrepel: Automatically Position Non-Overlapping Text Labels with
2182 “ggplot2.” (2024).

120. Yu, G., Smith, D. K., Zhu, H., Guan, Y. & Lam, T. T. ggtree: an r package for visualization and annotation of phylogenetic trees with their covariates and other associated data. *Methods Ecol. Evol.* **8**, 28–36 (2017).

121. Min, S. H. & Zhou, J. smplot: An R Package for Easy and Elegant Data Visualization. *Front. Genet.* **12**, 802894 (2021).

122. Barrett, T. *et al.* data.table: Extension of `data.frame`. (2024).

123. Gu, Z., Gu, L., Eils, R., Schlesner, M. & Brors, B. circlize implements and enhances circular visualization in R. *Bioinformatics* **30**, 2811–2812 (2014).

124. Forbes, S. PupillometryR: An R package for preparing and analysing pupillometry data. *J. Open Source Softw.* **5**, 2285 (2020).

125. Cao, J. *et al.* The single-cell transcriptional landscape of mammalian organogenesis. *Nature* **566**, 1–31 (2019).

126. Takata, K. *et al.* Induced-Pluripotent-Stem-Cell-Derived Primitive Macrophages Provide a Platform for Modeling Tissue-Resident Macrophage Differentiation and Function. *Immunity* **47**, 183-198.e6 (2017).

127. Meng, E. C. *et al.* UCSF ChimeraX: Tools for structure building and analysis. *Protein Sci.* **32**, e4792 (2023).